Towards a fully physical representation of snow on Arctic sea ice using a 3D snow-atmosphere model

David N. Wagner[1,2], David Clemens-Sewall[3], Markus M. Frey[4], Océane Hames[1,2], Mahdi Jafari[1], Amy R. Macfarlane[1], Adrien Michel[1,5],Martin Schneebeli[1], Matthew D. Shupe[6,7], Nander Wever[1], and Michael Lehning[1,2]

[1]WSL Institute for Snow and Avalanche Research SLF, Davos, Switzerland
[2]CRYOS, School of Architecture, Civil and Environmental Engineering, EPFL, Lausanne, Switzerland
[3]Thayer School of Engineering, Dartmouth College, Hanover, NH, USA
[4]British Antarctic Survey – Natural Environment Research Council, Cambridge, UK
[5]Federal Office of Meteorology and Climatology MeteoSwiss, Geneva, Switzerland
[6]NOAA Physical Science Laboratory, Boulder, CO, USA
[7]Cooperative Institute for the Research in Environmental Sciences, University of Colorado Boulder, Boulder, CO, USA

Key Points:

- A 3D-snow modeling setup including snow transport and temporally changing detailed snow properties was adjusted for Arctic sea ice.
- The model reproduces snow transport with high accuracy, and performed well in modelling the surface density with some uncertainty.
- The model will allow to investigate the insulating effect on spatial ice thermodynamics, especially in ridged areas.

Corresponding author: David N. Wagner, `wagner.david@posteo.net`

Abstract

Snow plays a crucial role in the heat transfer between the ocean and atmosphere in sea ice due to its insulating properties. However, wind-induced transport causes the snow distribution to be inhomogeneous, as snow forms dunes and accumulates mostly around pressure ridges and, leading to a heterogeneous underlying ice growth and melt. While models can help to understand the complex interactions of snow and sea ice, there is currently no 3D snow cover model for sea ice that considers detailed snow cover properties. This study presents the first application of the 3D-snow cover-atmosphere model ALPINE3D with the drifting snow module to Arctic sea ice. The model was calibrated and validated with measurements from the MOSAiC expedition. Wind fields used by the snow drift routine were generated with OpenFOAM which was forced by observations. A sensitivity analysis showed the impact of an increased fluid threshold on snow redistribution. The model performed well in simulating snow transport and mass fluxes, but underestimated erosion and poorly reproduced dune formation due to the missing dynamic mesh. The density was partially reproduced very well by the model, but uncertainties still exist in some cases. Comparing the surface snow density results with 1-D SNOWPACK simulations, ALPINE3D produced smaller differences but larger temporal variation in between setups. The study also investigated details of deposition and erosion using cross sections, showing good agreements of snow height differences between model and observations and revealing spatially high-resolution parameters such as age of deposited snow, density, and thermal conductivity.

Plain Language Summary

Snow affects the exchange of heat between the ocean and atmosphere in sea ice. It can insulate the underlying ice and affect how it grows and melts, but it is distributed unevenly by wind because the ice is often heavily deformed and wind also produces dunes. We used a computer model to simulate the distribution of snow on Arctic sea ice. We tested the model by comparing its results with measurements from the MOSAiC expedition. We found that the model performed well in simulating how snow is transported, but it underestimated erosion and was not able to accurately reproduce dune formation. ALPINE3D also computed the surface snow density, which showed at times good agreements with observations, but there are still some uncertainties. We compared the results with 1-D simulations from a model called SNOWPACK, and different ALPINE3D setups produced smaller differences in the end but a larger variation with time. The study also investigated details of deposition and erosion using cross sections, showing good agreements of snow height differences between model and observations and revealing information about snow age, density, and thermal conductivity. Overall, this study provides new insights into the complex interactions of snow and sea ice.

1 Introduction

The snow cover on Arctic sea ice forms a central element in the heat balance between the ocean and the atmosphere. On average, the snow cover in this area usually does not exceed 30 cm (Sturm et al., 2002; Wagner et al., 2022). However, due to its very high insulating capacity and high albedo, it may regulate the timing and speed of ice growth in autumn and winter, and melt in spring and summer (Nicolaus et al., 2006; Persson, 2012; Sturm & Massom, 2016). It further inhibits or delays ice melt during occasional warm-air intrusions that may occur even in winter (Persson et al., 2017).

Snow transport – the movement of snow particles due to wind – is initiated when a certain wind speed threshold is exceeded. This threshold depends on various processes, but mainly on vertical transport of horizontal momentum from the wind towards the surface and on the weight and the inter-granular bond strength of the snow grains. When this threshold is exceeded, grains may start to creep, going into saltation or suspension mode when wind speeds are higher (Bagnold, 1941; R. A. Schmidt, 1980; Melo et al., 2021).

Where wind speeds are lower, net deposition of the grains may occur and leading to surface accumulation. These drifts occur in the form of dunes (Filhol & Sturm, 2015) - or around obstacles. On sea ice, these obstacles are mostly pressure ridges formed by differential ice motion (Liston & Elder, 2006a). On a small scale, these drifts may determine how the ice grows and melts locally, e.g. they may modify the formation of melt ponds (Petrich et al., 2012; Lecomte et al., 2015). The snow cover and snow transport over sea ice have been investigated several times in the past. Déry and Tremblay (2004) modeled blowing snow transport including blowing snow sublimation over sea ice with the PIEKTUK model and focused on the effect of snow mass loss into leads on the mass balance. However, Déry and Tremblay (2004) did not make use of a saltation model, probably strongly underestimating horizontal mass fluxes. Leonard and Maksym (2011) modeled snow transport with the PIEKTUK model, as well, but with a saltation model in addition. The saltation transport threshold wind speed in this case was used as by Li and Pomeroy (1997), which is exclusively a function of the ambient temperature. Elevated temperatures lead to rapid sintering of the snow (i.e. increased formation of bonds between the snow grains) (Colbeck et al., 1997; Colbeck, 1998; Blackford, 2007) and therefore an increased threshold of wind-induced snow transport. The saltating mass flux itself is computed with the model from Pomeroy and Gray (1990). However, (Melo et al., 2021) showed in a model-intercomparison that this model underestimated the integrated mass flux significantly.

Liston et al. (2018, 2020) modeled snow transport in a very detailed way with their SnowModel, with statistically computed 2D-wind fields (Liston & Elder, 2006b) and a bulk-density snow cover representation. The core model for snow redistribution within SnowModel is SnowTran-3D (Liston & Sturm, 1998; Liston et al., 2007), whose threshold friction velocity is exclusively a function of a constant snow density (Liston et al., 2007). Liston et al. (2007) argue that this simple approach was sufficient for very low temperatures in winter in their studies, since a nearly constant surface-shear strength for the snow occurred under these conditions. However, they included the caveat that this approach may reach its limits for higher temperatures and detailed developments during snowstorms when more complex ambient conditions arise. SNOWPACK, a 1-D snow cover model applied recently to sea ice (Lehning et al., 1999; Wever et al., 2020), uses a saltation model to simulate snow transport if needed, which takes into account the surface properties of the temporally changing snow microstructure as well as the snow density (Doorschot & Lehning, 2002). Therefore, we believe that this approach could provide an advantage when studying snow cover on Arctic sea ice in a warming climate including warm air intrusions in winter, as well as during warmer months. In a saltation model inter-comparison, Melo et al. (2021) could show that with respect to integrated mass flux, the model from Doorschot and Lehning (2002) performed well for the tested specific bed types.

SNOWPACK has been applied in a distributed way in the form of ALPINE3D (Lehning et al., 2006), mostly for the Alps (Mott et al., 2010; Gerber et al., 2017; Schlögl et al., 2016), but for sea ice, as well (Wever et al., 2021). However, Wever et al. (2021) did not run the model with snow transport, i.e. without the SnowDrift module as presented in Lehning et al. (2008). Another approach recently applied to a sea ice topography was modelling snow transport with a gas-particle two-phase turbulent flow solver Hames et al. (2022). While the results regarding the locations of erosion and deposition are generally promising, no snowpack is implemented in the model; rather, the surface basically represents an infinite resource for snow mass, which itself does not represent an influence on the transport threshold because it does not represent any physical properties.

As already mentioned, ALPINE3D was mainly applied for larger Alpine scale simulations in the past. However, snow processes on sea ice are in principle not different than snow processes that occur in mountains, and there are only few snow models that are capable to conduct detailed snow transport modeling at this time. Hence, we built upon these previous studies by combining individual state-of-the-art methods as a novel approach of modeling of snow on sea ice, which – to our knowledge – has not been used in any other model setup so far:

- Detailed spatial modeling of the snow cover with very high resolution (dx, dy = 0.35 m) by means of SNOWPACK/ALPINE3D (Lehning et al., 1999, 2006).
- modeling snow saltation (Doorschot et al., 2004), suspension, erosion and deposition with ALPINE3D based on high-resolution Reynolds-averaged Navier-Stokes (RANS) equations based wind fields modeled with OpenFOAM (Weller et al., 1998).
- Making use of a very detailed digital elevation model (DEM) based on terrestrial laser scans (TLS) collected during the Multidisciplinary drifting Observatory for the Study of Arctic Climate (MOSAiC) expedition (Nicolaus et al., 2021) to have a realistic initial grid.
- Force the models with a detailed dataset of measured atmospheric parameters during the MOSAiC field campaign (Shupe et al., 2022).
- Validate the model with highly detailed spatial measurements of the height and density of the snow cover collected during MOSAiC as described in Nicolaus et al. (2021) and Wagner et al. (2022).

The goals of our study are to:

1. Calibrate and validate the model setup for the given conditions on sea ice during polar night.
2. Investigate the mass balance of snow.
3. Investigate how a changed snow transport threshold may lead to a change of transport rates and therefore a change in deposition/erosion patterns.
4. Evaluate the modelled snow surface density.

2 Methods and Data

2.1 Area and time selection

Snow- and atmospheric data was collected during the MOSAiC expedition (Nicolaus et al., 2021; Shupe et al., 2022) on sea ice in the high Arctic.

The exact study area on the ice floe and the time period were selected based on available observations that can be used to drive and evaluate the model. We also ensured that at least one drifting snow event occurred within this time period and TLS before and after the period were conducted, which required calm conditions. In addition, the topography in the study area should be sufficiently uneven in order for snow to accumulate. Hence, we decided for the 10-day long time period 25 Jan – 4 Feb 2020 (Fig. 1) covering the area of the northern transect (Fig. 2, a fixed track, which crossed an area consisting of second-year ice (SYI), on which snow depth measurements were taken weekly with high spatial resolution using a Magnaprobe (Sturm & Holmgren, 2018; Itkin et al., 2021; Nicolaus et al., 2021; Wagner et al., 2022)). Within this period, 4 more distinct drifting snow occurred, marked in yellow in Fig. 1. For this period, continuous meteorological measurements were available (Shupe et al., 2021, 2022), as well as one TLS on 25 Jan and one on 4 Feb for the northern transect area. In addition, occasional detailed snow cover and transect snow depth measurements were available for this area and period (Fig. 2). Based on drifting snow measurements with the snow particle counter (SPC) installed on the flux tower that was installed in the MOSAiC Central Observatory (Shupe et al., 2022) at 0.1 m above the snow surface we could determine the drifting snow periods. Detailed descriptions of the flux tower setup and snow measurements follow in a later section. In Fig. 1d, it can well be seen that one TLS was conducted on 25 Jan 2020 before the start of the drifting snow period and one after the drifting snow periods on 4 Feb 2020. The initial scan on 25 Jan 2020 was used to produce digital elevation models (DEMs) to be used as lower boundary topography for the model. The vertical difference between both scans is used to evaluate snow height distribution differences found in the simulations. It should precede the rest of the manuscript, that the conditions with 4 drifting snow events under different wind directions are not ideal for a calibration of the model, however, the aggravated conditions on the moving ice (Nicolaus et al., 2021) have to be taken into account, which rarely allowed for a referencing of the TLS at different days. We have been able to investigate two of these rare days here.

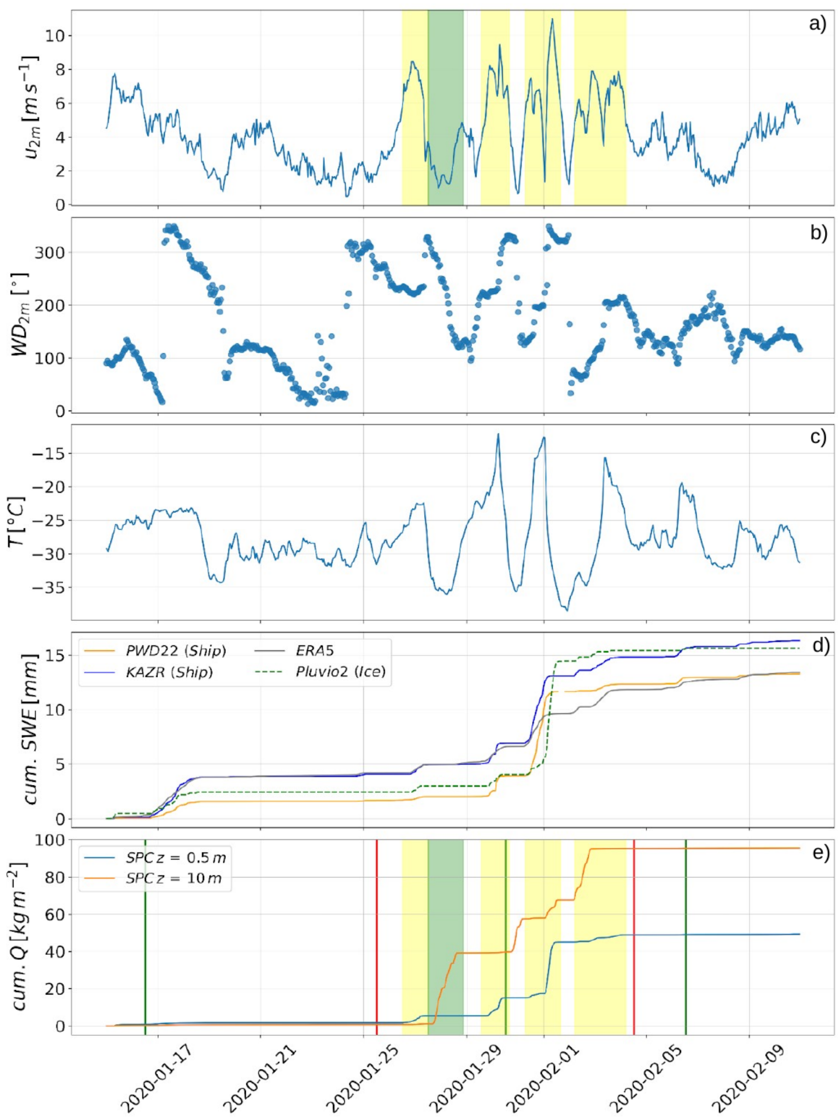

Figure 1. Time series of measured parameters between 16 Jan and 10 Feb 2020, for a) wind speed measured at 2 m height on the flux tower, b) wind direction with respect to the wind speed shown in a), c) 2 m air temperature at the flux tower, d) cumulative precipitation sums measured on the ship-based optical PWD22 sensor, retrieved from the K_a-Band Radar on the ship, ERA-5 reanalysis snowfall, Pluvio^2 pluviometer measured snowfall on the ice and e) cumulative horizontal mass flux for the snow particle counters (SPCs) on the flux tower, measured at 0.1 m and 10 m height, respectively. The green vertical lines in e) mark the days where transect measurements where conducted and the red vertical lines mark the days on which TLS were conducted in the same area. The yellow shaded areas in a) and e) mark the time periods of the drifting snow events. The green shaded area mark a suspicious increase of mass flux at the SPC installed at 10 m while wind speeds would theoretically not allow for snow transport. More details about snowfall measurements- and retrieval and SPC measurements can be found in Shupe et al. (2021); Wagner et al. (2022); Matrosov et al. (2022); Shupe et al. (2022).

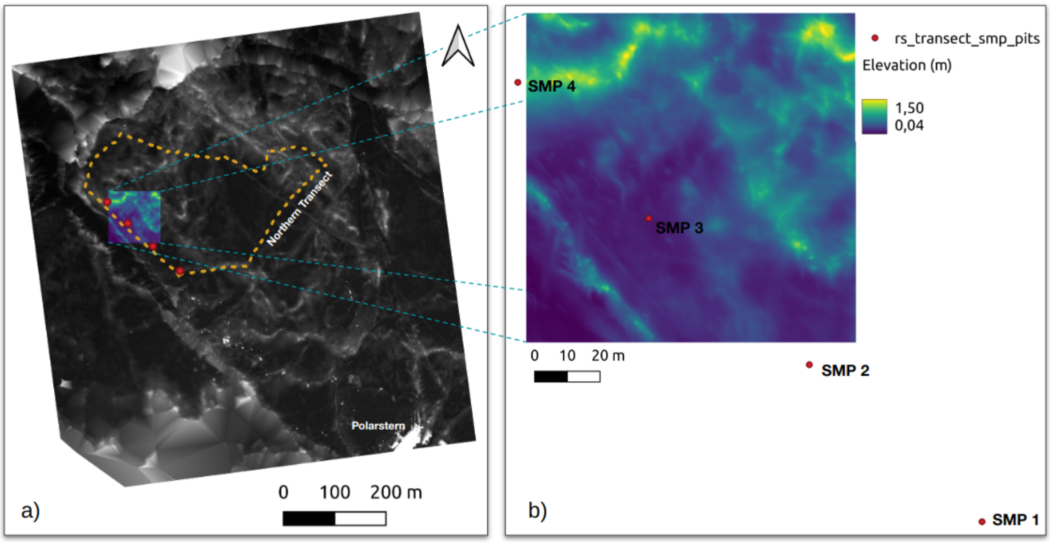

Figure 2. a) Shows the DEM derived from TLS on floe-scale, with the embedded model-domain. It also covers the northern transect and the location of FS Polarstern in the lower left corner. b) Shows the DEM on a smaller scale, including elevation magnitude and snow pit locations 1 – 4, where weekly SMP measurements were conducted.

2.2 DEM processing

TLS data was collected during the MOSAiC field campaign. Scans were conducted on 25 Jan and 4 Feb 2020 and referenced to obtain one large point cloud for each day in the same coordinate system (Clemens-Sewall et al., 2023). A cloth simulation filter (Zhang et al., 2016) was applied to the surface with CloudCompare (2023), in order to remove artefacts like flags, persons, tents or machines from the point clouds. In the following, the points were rasterized to a resolution of $\Delta x = \Delta y = \Delta z = 0.1\,\mathrm{m}$ in order to obtain a digital elevation model using the SAGA Geographical Information System (Conrad et al., 2015). Afterward, gaps were closed with spline interpolation, followed by applying a filter to remove further non-ground cells (Vosselman, 2000). Subsequently, a multilevel B-spline interpolation (Lee et al., 1997) and a multi direction lee filter (Selige et al., 2006) were applied in order to smooth the surface. These steps are essential in order to remove sharp edges that might lead to issues with grid generation or numerical instabilities in either OpenFOAM or ALPINE3D. The DEMs were aligned with respect to true north and squares with side lengths of 200 by 200 m were cut out. DEMs as shown for the TLS observation on 25 Jan 2020 (Fig. 2) were obtained. The lowest point in the DEM on 25 Jan was set to zero reference for all surrounding cells and also for the second scan on 4 Feb 2020. The DEMs show generally heterogeneous elevation, with a maximum height of 1.8 m on the highest ridges.

2.3 OpenFOAM wind field modeling

2.3.1 Mesh setup

Before the actual meshing, a horizontal flat buffer zone of 20 m width was added at each side with a smooth transition into the domain with the approach from Hames et al. (2022). This is necessary to avoid numerical instabilities under periodic boundary conditions. Afterwards, similar to Hames et al. (2022), to border the domain for the mesh, walls of 25 m height were added to each side and a top was added. Within these borders, a cartesian terrain-following mesh was generated using the cfMesh open source library

(Juretic et al., 2021) for OpenFOAM. The mesh consists of polyhedral cells in the transition regions where cell sizes are different and of hexahedral cells in the regions where cells sizes do not change anymore. The first layer above the ground has a height of 0.05 m, and the layer spacing as well as the horizontal cell size increases gradually with the distance from the ground. Further above, the cell size was set to Δx, Δy, Δz = 1 m. Even if 1 m seems relatively large, it should be sufficient for the low-turbulence areas well above the surface. The approach provided stable solutions and also has a lower computational cost. For the lateral boundaries, the patches were set to a cyclic Arbitrary Mesh Interface (AMI), which represents periodic boundary conditions.

2.3.2 OpenFOAM model settings and parameters

For wind field modeling, we used OpenFOAM® v2106 with the simpleFoam solver, which is solving the continuity and momentum equations for in-compressible, turbulent flow until a steady-state is obtained. To force the model, we used measured 1 h average wind data at 10 m height above the ice from the flux tower, for the time period 26 Jan – 4 Feb 2020. For each hour, that means one time step, 1 h average u, v and w components from 10 m were written into the OpenFOAM fvOption file as velocity which is translated into volume-averaged momentum source by the model. Hence, for each hour, an OpenFOAM simulation is ran until steady state of the vector field is reached. With this approach, short-term wind peaks, which certainly give strong impulses for the initiation of snow transport, are averaged out - however, we see this as the only reasonable approach if we want to calculate the snow transport itself in ALPINE3D also in hourly time steps. Once a steady-state solution is found for the domain-wide wind field, a new simulation starts with a new domain-averaged target wind vector. Thus we obtained a 3-D wind field for each hour. Additionally, we determined a constant roughness length of $z_0 = 5 \cdot 10^{-3}$ m as target roughness length in the model for the wall functions at the lower boundary for turbulent dissipation rate ϵ ($\mathrm{kg^2\,s^{-3}}$) and turbulent viscosity ν_t ($\mathrm{m^2\,s^{-1}}$), by comparing measured with modeled wind profiles and reducing its error (Fig. 3). Note that the comparison is limited, as we compare the horizontally averaged (height above the surface per layer) wind from the model with point measurements at the flux tower. The tower is not covered by the TLS scans (and therefore the model domain) for this period, it was located approximately 750 m south-east from the center of the domain. Furthermore, due to strong motion of the ice, the tower was quickly surrounded by high pressure ridges that affected the wind field. In addition, a hut was set up to the north-west, where the measurement data from various instruments were collected and pre-processed. Nonetheless, Weiss et al. (2011) found a median z_0 of $4.1 \cdot 10^{-3}$ m for Antarctic pack ice and 10^{-4} m for young ice, which is close to the obtained values from our comparison.

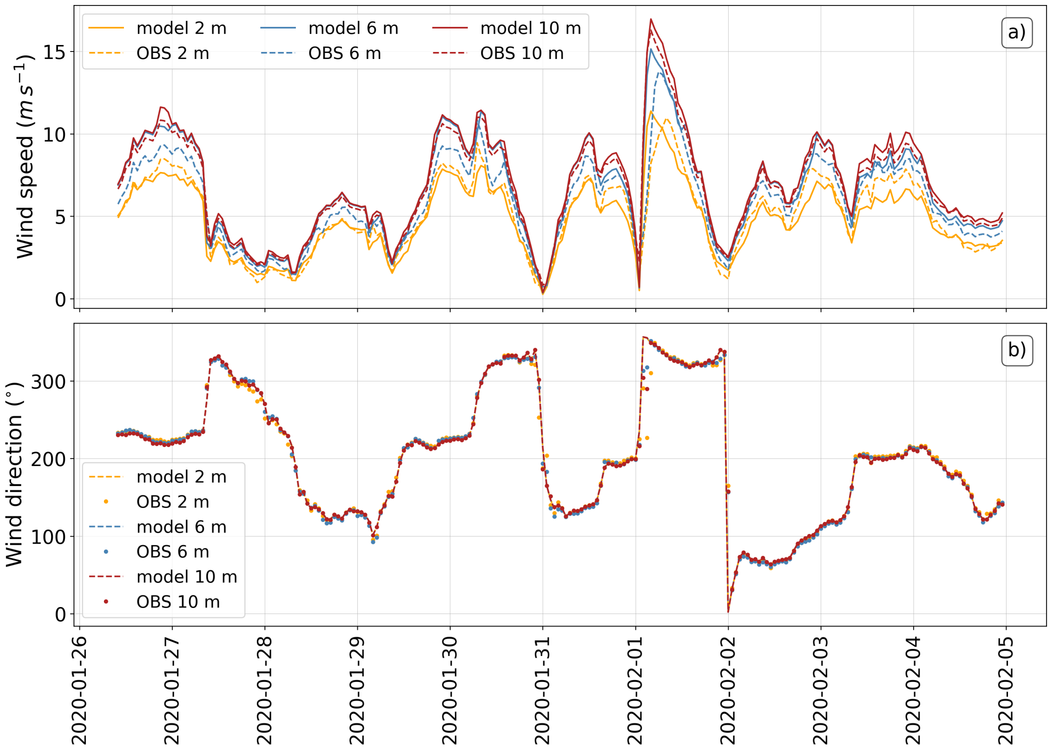

Figure 3. Comparison of wind measurements at the tower versus horizontally averaged model wind over time at the heights 2 m, 6 m and 10 m above the ice for a) wind speed and b) wind direction.

2.4 Snow cover and snow transport modeling

In order to conduct the actual snow cover- and transport modeling, we applied ALPINE3D (Lehning et al., 2008), which is a snow-atmosphere model using the 1-D layered SNOWPACK model for simulating the snow cover at each grid point (Lehning et al., 1999; Bartelt & Lehning, 2002). ALPINE3D enables to exchange surface mass fluxes and sublimation laterally between the connected grid cells. Its adjusted setup for sea ice is described in the following.

2.4.1 Meshing and wind field interpolation

As ALPINE3D requires a grid with hexa-hedral cells (Lehning et al., 2006, 2008), a new grid was required to be generated from the OpenFOAM unstructured mesh. To achieve this, we made use of the TerrainBlockMesher tool for OpenFOAM (J. Schmidt, 2014). By choosing cell increments (here: Δx, Δy = 0.35 m), a vertical spacing of 0.2 m close to the surface with an exponential increase and a vertical extent of $h(z) = 25$ m, TerrainBlockMesher reads the DEM of the sea ice and generates a structured grid on top which follows the terrain. The 3D wind fields from OpenFOAM were interpolated onto this structured grid with a Gaussian interpolation kernel by means of the PyVista Python library (Sullivan & Kaszynski, 2019). To run ALPINE3D, we chose a sub-section of the original DEM as shown in Fig. 2, a square with a side length of 100 by 100 m and a domain height reduced to 13 m which led to a 4-fold reduction in computation time when compared with the original domain size.

2.4.2 General model settings and parameters

The whole functionality of ALPINE3D is described in detail in Lehning et al. (2006, 2008). For saltation modeling, we applied the ALPINE3D-integrated saltation model from Doorschot and Lehning (2002). Although ALPINE3D's snowdrift routine is capable of computing sublimation of snow in suspension, we switched off that option, after finding only negligible differences. The reason is the small horizontal extent of the domain and the short time-span of the model run, leading to negligible snow mass sublimation in suspension for the meteorological conditions for the given time and location.

2.4.3 Meteorological Forcing

Besides the already described wind velocities, measurements of air temperature (measured at the flux tower at 2 m height), relative humidity with respect to ice (measured at the flux tower at 2 m height), precipitation rate ($\mathrm{mm\,h^{-1}}$) as retrieved from the K_a-band zenith radar (KAZR) installed on research vessel (RV) *Polarstern*, and incoming longwave radiation, measured near the flux tower, were used in the model. Note that no shortwave radiation input was required, as the research time period was during the polar night, without any incoming and outgoing shortwave radiation. General information about the MOSAiC atmospheric measurement setup including flux tower, radiation measurements, and KAZR can be found in Shupe et al. (2021, 2022). Detailed information about the KAZR can be found in Widener et al. (2012) while KAZR data can be found under Lindenmaier et al. (2020). The KAZR retrieval used in this paper follows Matrosov (2007); Matrosov et al. (2008) was applied by Wagner et al. (2022) and later evaluated by Matrosov et al. (2022) in detail.

2.4.4 Deposited snow density and microstructure

Regardless of whether it is new snow or previously eroded and redeposited snow, SNOWPACK uses the same parameterization for both density and microstructure with respect to this deposited snow. These parameters are calculated in ALPINE3D for each cell individually, mainly depending on the wind speed. For the deposited snow density ρ_n, we applied the following formula, adapted from Groot Zwaaftink et al. (2013)

$$\rho_n = \begin{cases} \rho_1 \cdot \log_{10}(U) + \rho_0, & \text{if } U \geq 1 \\ 33, & \text{otherwise} \end{cases} \tag{1}$$

where U is the instantaneous wind speed at a grid cell. For ρ_1 we set $361\,\mathrm{kg\,m^{-3}}$ as in Groot Zwaaftink et al. (2013) and $\rho_0 = 33\,\mathrm{kg\,m^{-3}}$ in order to allow low snow densities at very low wind speeds. Contrary to Groot Zwaaftink et al. (2013), we also did not apply long-term averaged wind speeds in the formula but instantaneous wind speeds at each grid cell.

We further applied the POLAR variant of SNOWPACK which comes along with further surface compaction mechanics due to wind and changes in the snow settling which are described in Groot Zwaaftink et al. (2013); Steger et al. (2017).

For the deposited snow microstructure, in the POLAR variant, compared against the DEFAULT variant, various deposited snow properties differ, partially depending on the wind speed. In general (independently of the wind speed), the new snow sphericity is increased (0.75) compared to the DEFAULT variant (0.5), while the dendricity is decreased (0.5 vs. 1.0). At high wind speeds ($> 5\,\mathrm{m\,s^{-1}}$), the sphericity is increased even further (1.0 vs. 0.75) while the dendricity is decreased further (0.15 vs. 0.5), reflecting mechanical destruction of grains from transport by wind. Further, new snow bond size gets stronger with a factor of 3 compared to the DEFAULT variant. The POLAR variant also exhibits a stronger compaction of the near surface layers by wind, by applying a magnifying factor. In addition, we applied a factor of 5 that is multiplied in addition to favor wind slab formation.

2.4.5 Fluid threshold

The drifting snow routine from ALPINE3D (Doorschot & Lehning, 2002) is computing drifting snow mass flux based on a fluid threshold shear stress initiating snow grain motion τ_{th} (Pa) determined as:

$$\tau_{th} = A\,\rho_i\,g\,r_g\;(\psi + 1) + B\,\sigma\,N_3\,\frac{r_b^2}{r_g^2} \tag{2}$$

where $A = 0.023$ and $B = 0.0035$ are empirically determined constants (Clifton et al., 2006), $\rho_i = 917\,(\mathrm{kg\,m^{-3}})$ is the density of ice, $g = 9.81\,(\mathrm{m\,s^{-2}})$ is the gravitational acceleration, r_g is the grain radius in m, r_b is the bond radius in m, ψ is the sphericity of snow grains which can be between 0 and 1, $\sigma = 300\,(\mathrm{Pa})$ is an empirically determined bond strength and N_3 is the three-dimensional coordination number.

The threshold friction velocity which must be exceeded by the wind at the surface to initiate snow transport is defined as:

$$u{*}_{th} = \sqrt{\frac{\tau_{th}}{\rho_a}}, \tag{3}$$

where $\rho_a = 1.1\,\mathrm{kg\,m^{-3}}$ is the density of air.

In order to investigate the dependence of the snow redistribution on the strength of the fluid-threshold in the further course of the work, we introduce the factor α, which allows us to scale the fluid threshold:

$$\tau_{th}^{*} = \alpha\,\cdot\,\tau_{th}. \tag{4}$$

For the base setup, we kept α at 1.0, which we called reference setup (R). However, we also performed simulations with $\alpha = 3.0$, which led to changes in the mass balance and density, which we would therefore like to present in addition. In the following, we call these simulations comparison scenario (C).

2.4.6 Mass balance treatment

The ALPINE3D drifting snow routine (Doorschot & Lehning, 2002) computes for each time step a global steady state condition for the location of snow mass in the air. The location and magnitude of eroded mass that is entrained into the air (and deposits somewhere else) depends on the fluid threshold that is explained in section 2.4.5. Hence, at each pixel in the domain, a SNOWPACK simulation returns the amount of snow eroded/deposited at each time step to the ALPINE3D model kernel. The drifting snow routine can only erode one snow layer at a SNOWPACK model timestep, which is 15 min. in this study. As the computed amount of mass in the air depends on the snow properties of the uppermost snow layer, deeper layers can exhibit a stronger bond and higher density, reducing the erosion. In this approach, at a certain cell, the computed eroded mass may be greater than either the actual available mass of the surface layer. It might also be the case that the total mass on the ground is less than the eroded mass computed by the drifting snow routine. In both cases, the suspended (and later deposited) mass is greater than the total snow mass actually available for erosion. In addition, since precipitation is consumed in the drifting snow routine and snow is allowed to remain in suspension, snow might never be deposited and the deposition rate might be lower than the precipitation rate. In order to close the mass balance, the following approach was implemented in the model:

1. For each pixel and time step, the erosion mass returned by the drifting module is limited to the mass of the uppermost layer.
2. The global mass balance, i.e. the deposition plus the precipitation minus the corrected erosion is computed.
3. If the mass balance is positive, the deposition is linearly decreased for all pixels in order to obtain a zero value for the mass balance. If the mass balance is negative, the deposition is linearly increased for all pixels in order to obtain a zero value for the mass balance.

At deposition time, the density of deposited new snow is set to the deposited snow density (Section 2.4.4).

2.4.7 Snow cover measurements

SnowMicroPen (SMP) resistance force measurements (Schneebeli & Johnson, 1998) conducted at the same four positions along the Northern transect at around 12 UTC on 16 Jan, 30 Jan and 6 Feb (Fig. 2). At each location and on each day, 5 measurements were conducted. Out of the collected force profiles, densities were computed as by King et al. (2020) Wagner et al. (2022) and the 5 density profiles were averaged after aligning with the snow surface. Out of the four positions, only the profile of SMP3 was covered by the model domain (Fig. 2b). The surface density determined in this way will be used for comparison with the model.

In addition, a Magnaprobe (Sturm & Holmgren, 2018) was used to measure snow depths along the Northern Transect on a weekly basis, ice and weather conditions permitting. The methodology of the measurements and the data set are described in detail by Itkin et al. (2021). Furthermore, we derived snow depths from the SMP measurements. We use the snow depth data from both instruments to compare the differences between the individual days with those of the model.

2.4.8 Initial snow cover

To initialize the ALPINE3D snow cover, we first created a snow profile for SNOWPACK based on an horizontally averaged SMP density profile measured on 16 Jan from all the SMP1 – SMP4 locations, on the northern transect (Fig. 2b). The 20 single profiles were first aligned along the surface and made an horizontally averaged profile. As the middle part of the profile was mostly vertically constant in terms of density but not the lowest part (due to temperature gradient metamorphism) and the most upper part (due to wind compaction), and in order to get the best estimate for temperature and density, we extracted the upper 11 cm and the lower 11 cm of this average profile and created an initial SNOWPACK composite profile out of the extracted upper and lower part. The average density of the initial profile is $285\,\mathrm{kg\,m^{-3}}$. With this profile, we made a single (1D) SNOWPACK spin-up run until 26 Jan 1000 UTC forced by the meteorological measurements. The density state on 26 Jan 1000 UTC of the profile is shown in Fig. 4. The increase of snow height between 16 and 26 Jan is only 1 cm, which corresponds to 1.3 mm of SWE. The profile properties are rather constant with height, however with a slightly decreased density toward the bottom due to depth hoar formation and a wind slab at the top. The profile mostly consists out of depth hoar in the lower part (dark blue in Fig. 4), faceted grains (light blue) in the upper part, a layer of rounded grains (magenta) in the upper part as wind slab. This profile out of the spin-up was then distributed uniformly over the ALPINE3D domain and is used as initial state on 26 Jan 1000 UTC. The total height of the initial profile (23 cm) is approximately consistent with the average snow depth of the northern transect measured with the Magnaprobe on 30 Jan (26.7 cm).

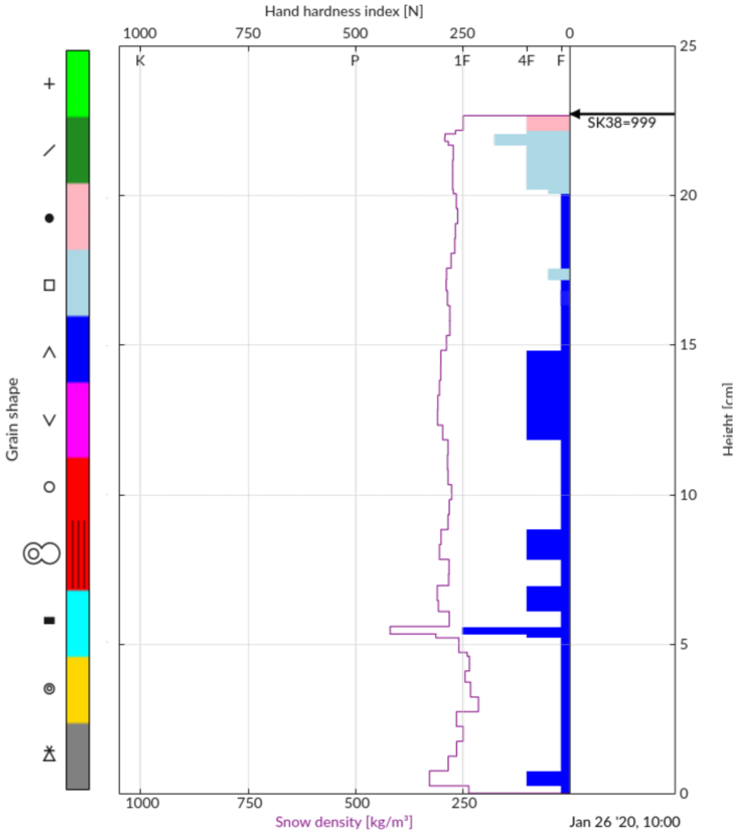

Figure 4. The initial profile after spin-up at 26 Jan 1000 UTC, which was distributed over the domain as ALPINE3D initial snow cover state at each grid cell. The colors indicate the grain shapes as classified by Fierz et al. (2008), where the legend on the left describes the relationship between the shown colors and grain type symbol.

2.4.9 1D SNOWPACK simulations

In order to investigate whether the computationally expensive ALPINE3D setup offers advantages over a computationally very cost-effective 1D SNOWPACK simulation with regard to the calculation of the surface density, we set up 2 SNOWPACK simulations for comparison, which we ran from 16 Jan based on the initial profile (Section 2.4.8). Both simulations were set up with the same settings as R and C - only 1-dimensional - therefore they are called SP_R and SP_C in the following.

3 Results and Discussion

3.1 Drifting snow mass fluxes

In the following, we evaluate the model in terms of snow transport SPC measurements, which took place at the same flux tower as the wind measurements used to drive the model. To make a comparison possible, we defined a normalized mass flux for the lower SPC at 0.1 m above the surface simply as a ratio of instantaneously measured mass flux relative to the maximum measured over the whole investigation period. For the model, we used the spatial average of the instantaneous absolute values at each grid cell with respect to deposited and eroded saltation mass (kg m^{-2}). As for the SPC, we normalized the averaged absolute saltating mass. By doing so, we are able to compare the timing of snow transport as well as the relative magnitudes with the measurements. The normalized mass flux, measured at the lower SPC at 0.1 m above the surface, is very well represented by the normalized mass flux in the reference model setup (Fig. 5c,d). The frequency distributions of measured mass flux at the 0.1 m SPC versus the modeled mass flux plotted as a wind rose (Fig. 6) indicate well simulated mass flux with respect to wind direction, as well. Note that the ratio in the NNW sector is under-represented in the model. The reason is probably that in reality the SPC was wind-shadowed by relatively high ridges in the NNW sector and the mentioned installed hut, leading to under-sampling of drifting snow particles for this wind direction.

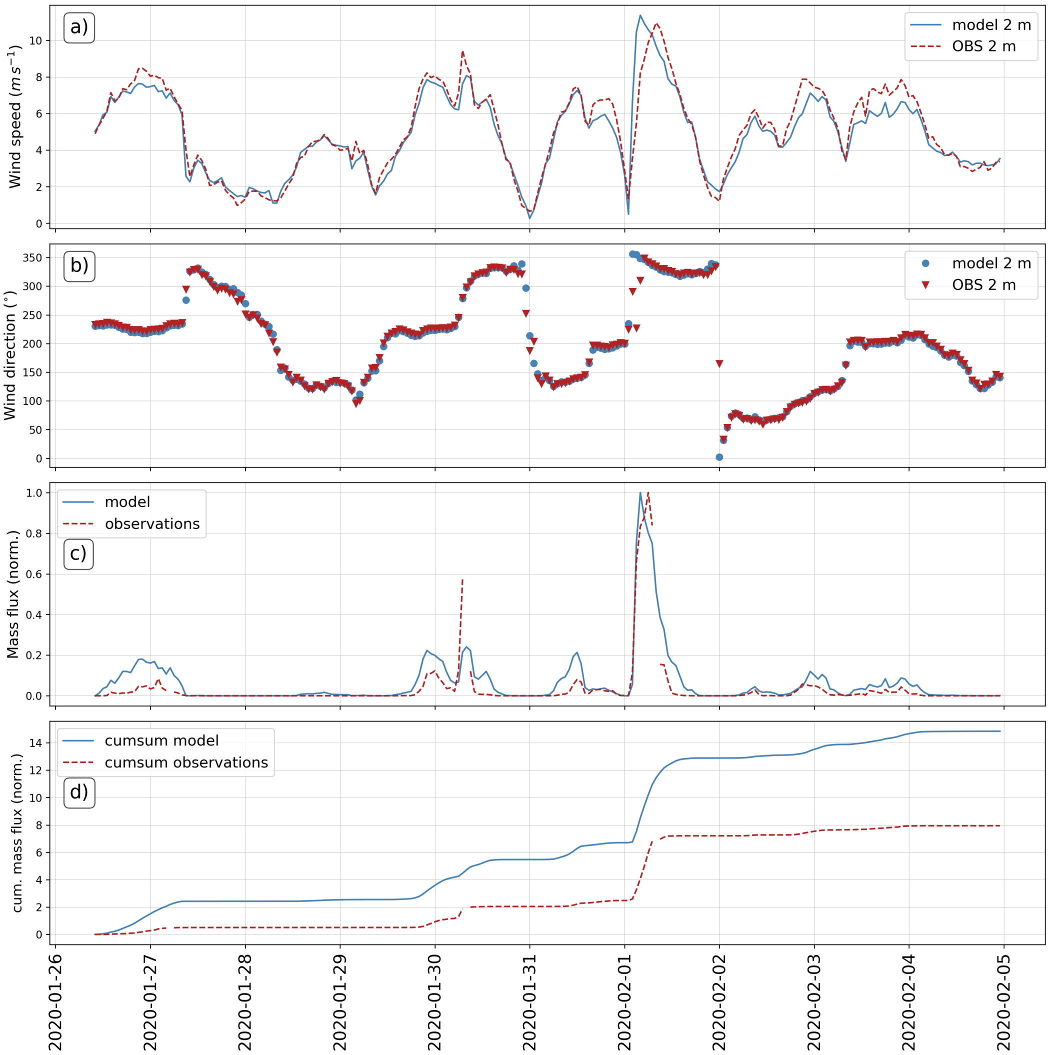

Figure 5. a) 2-meter tower-observed wind speed (1 h avg) versus horizontally averaged 2-meter modeled wind speed from OpenFOAM. b) Same as for a), but for wind direction, c) modeled (R) and measured normalized drifting and blowing snow mass flux over time. d) modeled (R) and measured cumulative normalized drifting snow mass flux over time.

However, also note that average (domain-wide) modeled mass flux is compared with point measurements that were measured a few hundreds of meters away from the area that is represented in the model. In addition, the SPC was partially wind-shadowed by ridges in its Western and North-western direction, making accurate absolute comparisons very difficult.

Nevertheless, the results show that the model can be used to determine the timing of drifting snow events and relative mass flux with very high accuracy ($r = 0.92$).

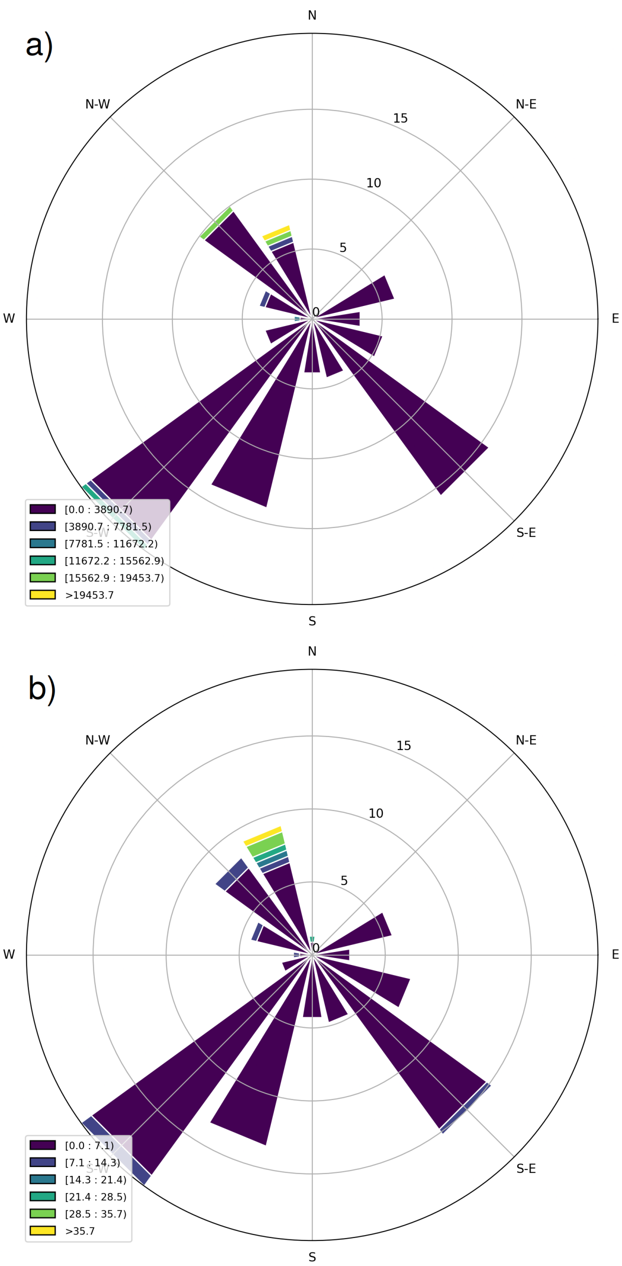

Figure 6. a) Wind rose for the measured mass flux with the lower SPC (0.1 m). b) Wind rose for the modeled spatially averaged absolute saltation deposited and eroded flux.

3.1.1 Potential uncertainties regarding the drift threshold

It is noteworthy that A and B in Equation 2 are empirically determined. We choose the values as used by Clifton et al. (2006) ($A = 0.023$ and $B = 0.0035$). However Keenan et al. (2021), for instance used the parameters $A = 0.02$ and $B = 0.0015$ as it was recently implemented in SNOWPACK. In our case, we found a tendency of the model to compute the initiation of saltation at too low wind speeds relative to the measured mass flux, extending the drifting snow time periods in the model over the measured ones. Hence, as increased A and B parameters increase the fluid threshold, we chose to use the older values.

Note, that the surface snow density - hence the used deposited snow density parameterzation (Equation 1) is indirectly affecting the fluid threshold, and therefore the re-distribtion. The coordination number N_3 - a factor in the second term of the fluid threshold equation (Equation 2) - fitted by Lehning et al. (2002) and used in the recent SNOWPACK version in the following form, is directly dependent on the bulk density of snow ρ_s:

$$N_3 = 1.42 - 7.56 \cdot 10^{-5}\rho_s + 5.15 \cdot 10^{-5}\rho_s^2 - 1.73 \cdot 10^{-7}\rho_s^3 + 1.81 \cdot 10^{-10}\rho_s^4. \tag{5}$$

Hence, the adjusted deposited snow density is affecting directly N_3 and hence indirectly affecting $u*_{th}$ (Equation 3), leading to an increased $u*_{th}$ with increasing density.

Since only wind measurements took place outside the model domain, we were only able to fit wind speeds in the model as domain-average to the measurements from a station slightly outside the model domain. Thus, the model wind profile may not fit the measurements well in every case. Furthermore, the values for A, B and σ were found empirically, either in a wind tunnel or from experiments in the Alps. In fact, general wind- and environmental wind conditions are quite different to conditions in the Alps and most likely, wind tunnels as well. In addition, there are several other factors, like the particle entrainment coefficient, where the value currently used in SNOWPACK has been found empirically (Groot Zwaaftink et al., 2014) at it is likely that the environmental conditions during that study do not resemble those of our study. Hence, several other empirical fitting parameters are not necessarily correct for snow on sea ice, as well.

3.2 General mass balance

In this section we want to examine the following points, related exclusively to the parameter of the snow depth difference:

1. Investigate basic spatial statistics of the modeled snow height differences and how it compares to the measurements.
2. Conduct spatial correlations of snow height differences compared to model measurements and compared to previous studies on sea ice (Sturm et al., 2002; Liston et al., 2018).
3. Do a qualitative evaluation of spatial differences model versus observation.
4. Having a statistical view on the spatio-temporal change of snow distribution in the model.

3.2.1 Frequency distributions of snow height differences

The frequency distribution of the spatial snow depth difference between the two laser scans can well be described by a Cauchy distribution (Fig. 7a).

In order to evaluate the spatial snow distribution of the various model runs quantitatively with time, first we generated maps of 2-dimensional snow depth differences $\Delta HS_{i,j,t-t_0}$ for both, model output and TLS:

$$\Delta HS_{i,j,t-t_0} = HS_{i,j}(t) - HS_{i,j}(t = 0). \tag{6}$$

where $HS_{i,j}(t)$ is the total snow height at each point of the grid at time t, with i, j being the horizontal indices for the grid points in x and y direction, respectively, and $HS_{i,j}(t = 0)$ is the total snow height at each point of the grid at time $t = 0$.

In Fig. 7a we see that the distribution is almost symmetrical along the y-axis, however, also slightly skewed. The location on the x-axis x_0 also indicates that the peak is slightly shifted toward negative values.

The distribution is generally well reproduced by the model (Fig. 7a). However, the modeled distribution is rather described by a a Gaussian than a Cauchy distribution as observed. Especially, it is noticeable that the negative range of the distribution is less pronounced for more negative values, which indicates less area of erosion for higher depths in the model.

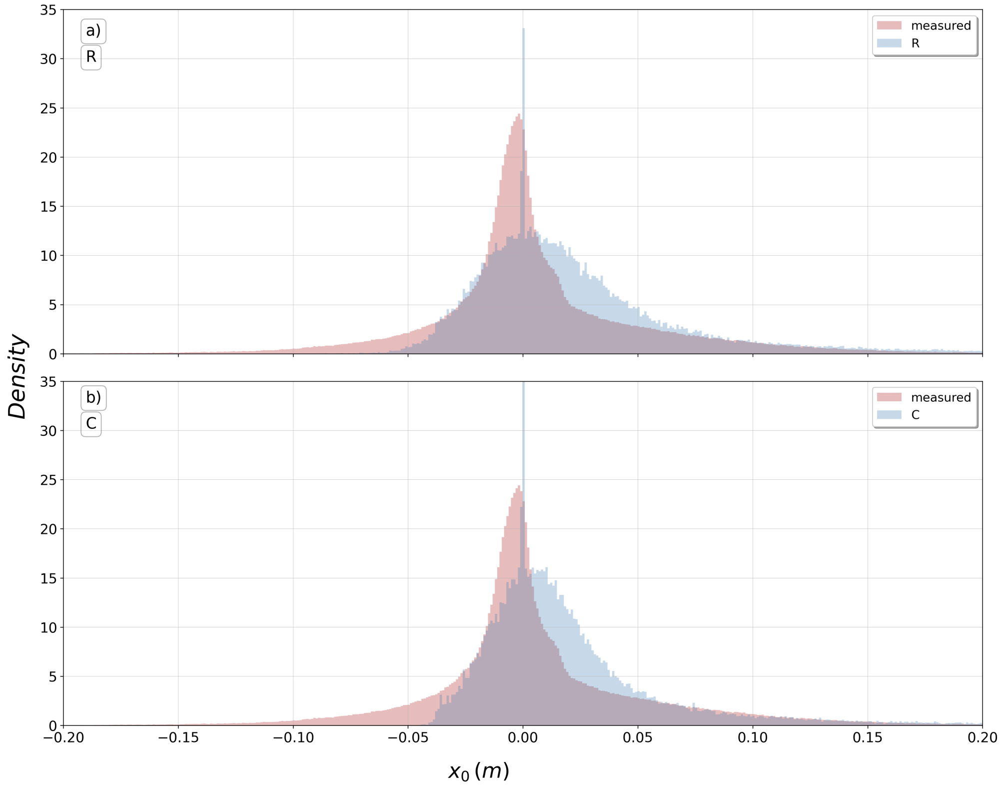

Figure 7. Frequency distributions for modeled snow depth differences between first and last hour of the model output and TLS measured difference. a) shows the reference, b) the C scenario

One reason for this could be the neglect of the spatial variability of the snowpack in the initialization of our model. Areas where snow drifts were deposited shortly before 25 Jan will be relatively easier to erode than snow that has deposited earlier and sintered for a longer time. The negative tail in the observations could be the erosion of these recent drifts. Because the model uses uniform snow properties, it does not resolve these recent drifts and hence misses the negative tail. Hence, bringing the distribution from the model output in closer agreement with observations is very difficult, if not impossible, as we not only had to guess the initial distribution of snow mass but also the distribution of the snow properties based on point measurements.

Compared to the R scenario, the C scenario with $\tau^*_{th} = 3.0$ (Fig. 7b) shows a less compressed distribution, but also with less pronounced legs to the sides. For us, this is an indicator that less redistribution has taken place in the C scenario due to the higher fluid threshold.

3.2.2 Statistical view on the spatio-temporal change of snow distribution

The model enables the detailed study of events within the time-span of two laser-scans. To examine the temporal evolution of the spatial distribution in detail statistically, we consider histogram time series for the modeled snow depth difference of the reference scenario (Fig. 8a) versus the comparison scenario (Fig. 8b) based on Equation 6. Although we detected 4 main drifting snow events within the investigation period initially by means of the measurements (Fig. 1), the histogram time series of the reference (Fig. 8a) shows that the snow cover in the simulation was affected by re-distribution most of the time. However, simulation C shows muss less dynamics (Fig. 8b), and the distinct events for this setup can mainly be reduced to the 4 main events as detected solely with the measurements. This raises the question which scenario is more realistic - relative mass flux comparisons (Fig. 5c) suggest that the mass flux for the reference run was too high. From this we conclude that the redistribution in the C scenario is probably more realistic. A detailed verification over time does require a significantly higher frequency of measurements of the snow depth difference.

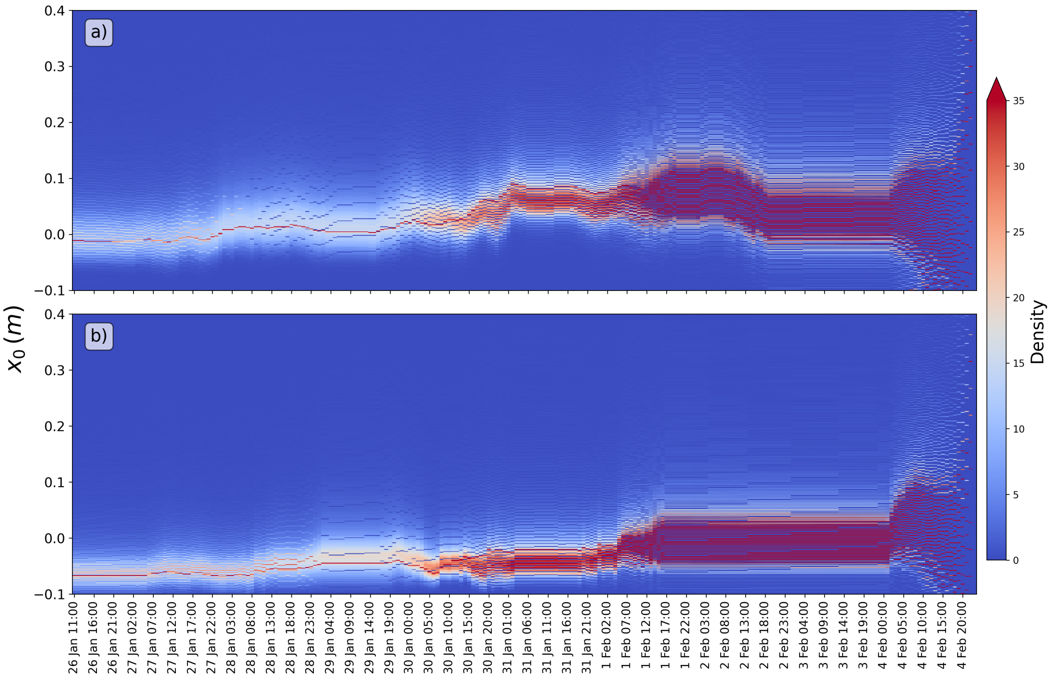

Figure 8. 2-D time series of the frequency distributions as shown in Fig. 7a, for a) R scenario and b) for the C scenario. Each time step shows one histogram for the difference of snow depth at the time with respect to the snow depth at $t = 0$. The color indicates the density.

3.2.3 Spatial correlation

To evaluate the spatial correlation of snow depth differences, we can look at semi-variograms, which have been generated using the Python SciKit-GStat library (Mälicke, 2022). To estimate the semi-variance, we used a Matheron estimator function (Matheron, 1963):

$$\gamma(h) = \frac{1}{2N(h)} \sum_{i=1}^{N(h)} \left(x(P_i) - x(P_{i+h}) \right), \tag{7}$$

where N (h) is the number of point pairs for the lag distance h (in meter), and x (in meter) is the observed value at its location P. Hence, semi-variograms describe the spatial correlation of point pairs as a function of their distances from each other. The computed semi-variogram for the snow height difference of the observation and the R scenario is shown in Fig. 9a. The measured difference has a smoother transition from highest correlation towards least (constant) correlation, which is reached at a range of approximately 6 m distance. The transition towards least correlation in the model is less smooth, though also reached at approximately 6 m distance. The correlation decrease occurs fast in the model, with a quick decrease from 0 to 2 m distance, and less decrease from 2 m onward. The differences between reference (Fig. 9a) and comparison scenario (Fig. 9b) are not large, although a generally larger positive deviation of the semi-variance is observed for the comparison scenario for the whole lag distance.

We expect a less smooth transition from high towards low (steady) correlation to be a result of less long-stretched deposition and erosion patterns in the model output. The reason could be that our grid is static and does not dynamically adapt to the snow surface over time. In order to get the model to produce dunes, an adaptive mesh that accounts for newly deposited or eroded snow at each time step, would be required. This is not implemented in the current setup.

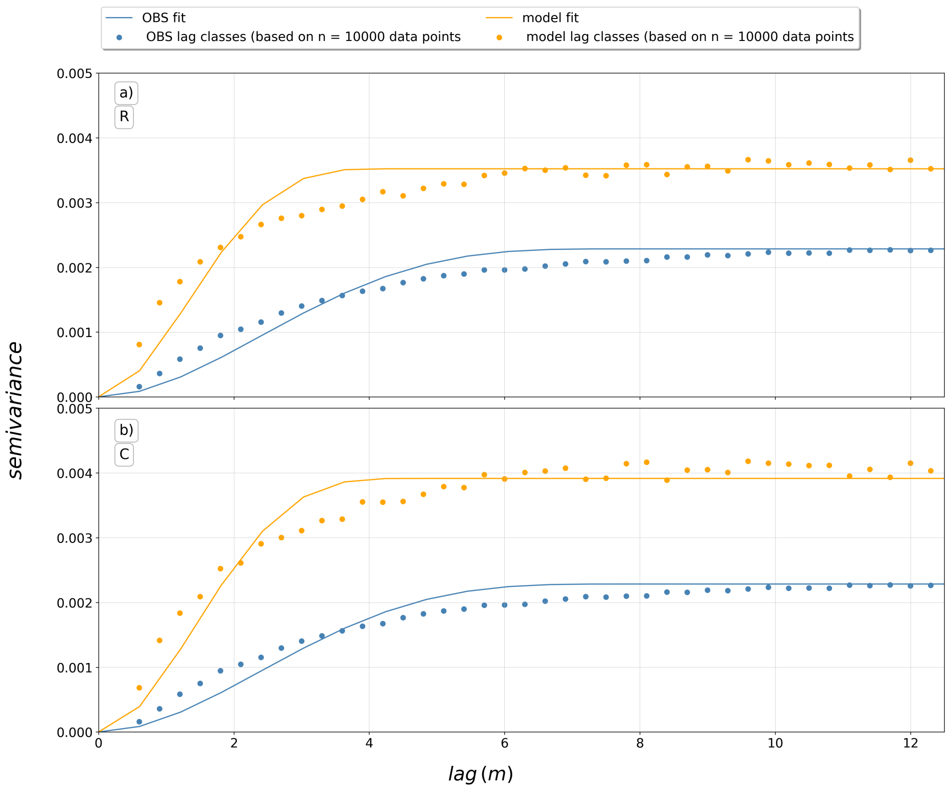

Figure 9. Semi-variance for modeled snow depth differences between first and last hour of the model output and TLS measured difference for a) the reference scenario R, b) scenario C.

It is noteworthy that, in a qualitative comparison, ranges of semi-variograms for absolute snow depth distributions over Arctic sea ice compares with other studies on Arctic sea ice (Sturm et al., 2002; Liston et al., 2018). Liston et al. (2018), for example, examined semi-variograms based on snow depth measurements along various transects measured during the Norwegian Young Sea Ice Experiment (N-ICE2015) field campaign and a snow cover model which models the snow height spatially for the respective same area. For both the measurements and the model, a range of almost 6 m was observed, similar to our results. Sturm et al. (2002), on the other hand, examined semi-variograms based on snow depth measurements along various transects during the Surface Heat Budget of the Arctic Ocean (SHEBA) campaign of the years 1997-1998. Here, mostly larger ranges between 13 and 30 m were found, but most of them in the lower end of this range. Since we compare snow depth difference in our case with absolute snow depth in the other two studies, the absolute values of the semi-variance are logically of different magnitudes. However, it is clear that during our measurements, and the measurements during SHEBA, fundamentally different snow conditions prevailed. Webster et al. (2014), for example, has calculated that between the years 1950 and 2014 the mean snow depth on Arctic sea ice decreased by 2.9 cm per year. If we now look at the relatively large mean snow depths at the end of the winter season during SHEBA (33.7 cm) and extrapolate over the value would arrive at 27.4 cm for MOSAiC, which is not far from the measured value from Wagner et al. (2022) (24.9 cm). In addition, Merkouriadi et al. (2017) reports strongly different proportions of depth hoar or faceted grains and wind slab in the snowpack for N-ICE2015 compared to SHEBA and Sturm et al. (2002) reported consistently low temperatures that favored the development of depth hoar, while both Merkouriadi et al. (2017) reported warm air intrusions in winter, as did Shupe et al. (2022) for MOSAiC. Overall, then, we must assume that snow conditions differed greatly, particularly between SHEBA and N-ICE2015 or MOSAiC.

Nevertheless, the strong similarity of the values between (Liston et al., 2018) and our study suggest that snow conditions were more similar between N-ICE2015 and MOSAiC, especially in terms of spatial snow distribution.

3.2.4 Qualitative evaluation of spatial differences

Spatial correlations allow for quantitative comparisons, however, they do not reveal all properties of spatial variation. Therefore, qualitative comparisons with respect to the localization of drifting snow patterns are made in the following section.

Absolute snow height outputs for the R and the C model are shown in Fig. 10a and Fig. 10b, respectively. Surface densities (discussed later) are shown in Fig. 10c,d. Overall, higher maximum snow heights can be observed for the C scenario (Fig. 10b). We assume that this is due to initially precipitated snow (precipitated under conditions when snowfall and wind prevail at the same time) that is less prone to erosion and therefore removal.

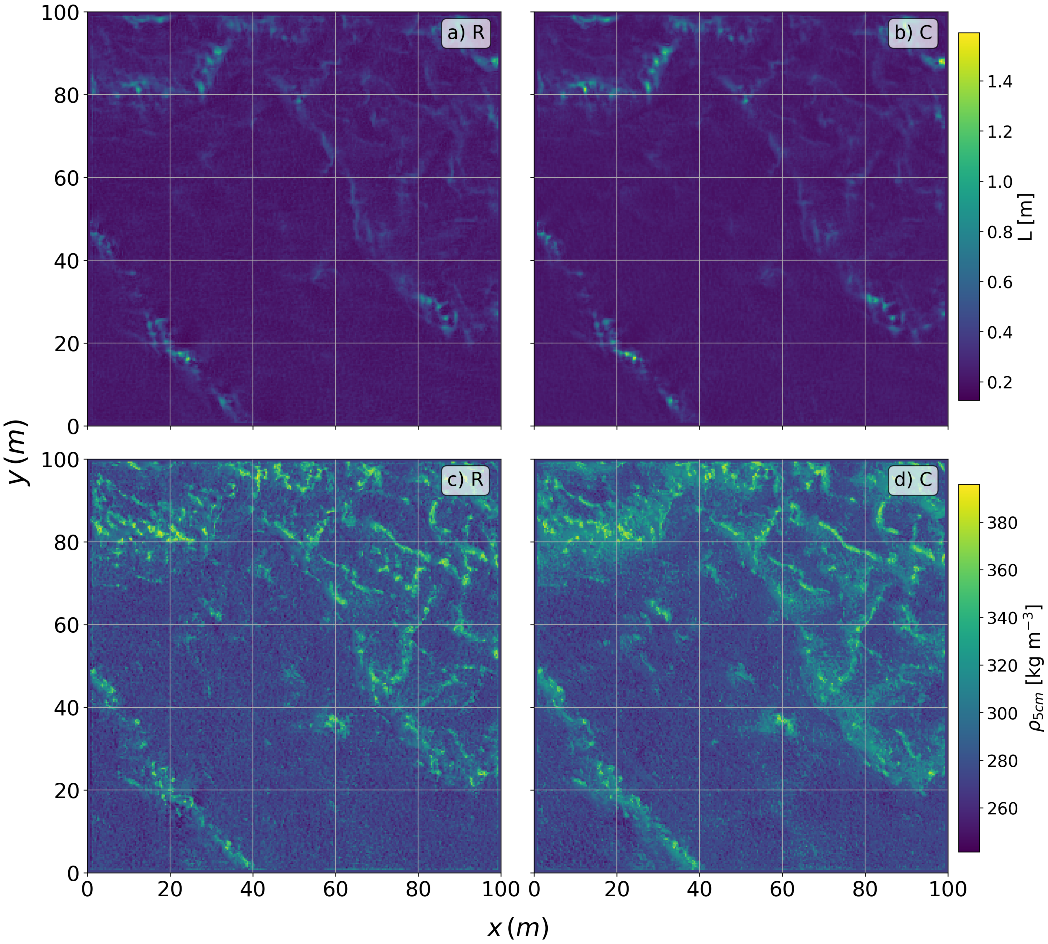

Figure 10. a) modeled (R) absolute snow height, b) modeled (C) snow height, c) modeled (R) surface density $\overline{\rho}_{5cm}$ and d) modeled (C) surface density $\overline{\rho}_{5cm}$.

The comparison of the spatial distribution of absolute snow depth differences between model reference and TLS measurements is shown in Fig. 11a,b. Purely visually, the spatial distribution does not appear to be particularly well reproduced by the model. In addition, as already mentioned, dunes in flat areas are almost not reproduced. However, there are locally good model results, and examples for this are marked in orange circles. In addition, as in the TLS observations, snow mass is preferably deposited along the distinct ridge in the lower left corner of the domain - although the specific locations and scales of the deposited mass are different from those that are observed. Erosion does occur in the model as well, although at a much lower magnitude than observed, especially around the distinct ridge. Correlations and anti-correlations between model and TLS can also be observed, which depend primarily on the topography. Besides the ridge at the bottom left of the domain, stronger structures at the top left are visible in both the model and the TLS. The same is true for an edge that runs from about x = 40, y = 90 to x = 100, y = 20. However, this edge is clearly of an anti-correlative nature. The reasons for this are currently unknown. Another location where erosion and deposition is well reproduced in the model is cross section S1 (discussed in detail in Section 3.4.1. We further will look into detail at cross section 2 and cross section 3. In order to see if the total accumulated snow is affecting the patterns visually, we normalized the absolute distributions for model and TLS respectively (Fig. 11c,d), i.e. the respective difference values at each index point were divided by the highest difference value per domain.

In this representation, the differences between the model and TLS are no longer quite so drastic.

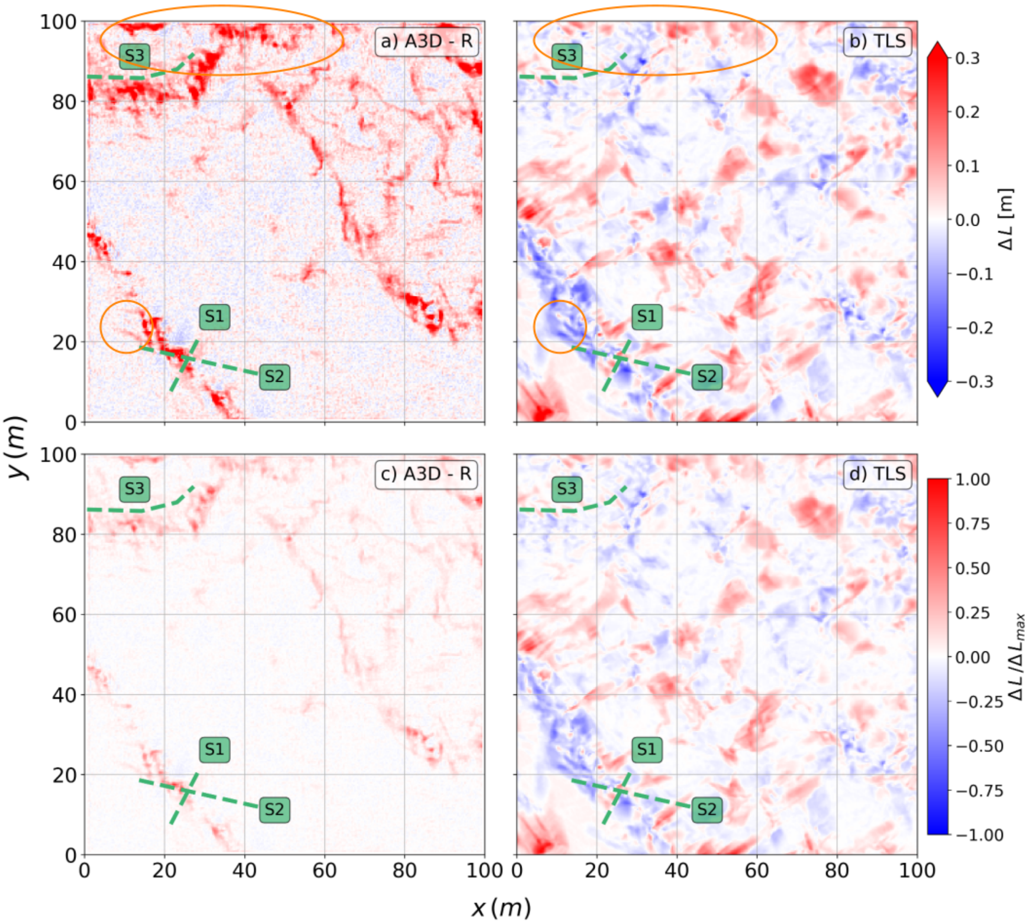

Figure 11. a) modeled snow depth difference between 26 Jan and 4 Feb for the R model run, b) is the measured snow depth difference via TLS between 26 Jan and 4 Feb, c) shows the modeled normalized snow depth difference for the R model run and d) shows the measured normalized snow depth difference from the TLS.

3.2.5 Time series averages and comparisons with 1-D SNOWPACK simulations

For a more detailed view of individual domain-averaged model parameters, we look at Fig. 12. Here, the individual events are more clearly visible for both, the reference and C scenario (Fig. 12). As expected, the C scenario ($\tau^*_{th} = 3.0$) does most of the time produce lower snow transport rates, but partially even computes higher transport rates in comparison. This is valid for a short time span on the 30 Jan and on 1 Feb. Reasons for this rather uncommon behaviour still need to be investigated. Averaged snow height differences of the ALPINE3D C and R scenarios and their standard deviations, as well as two 1-D SNOWPACK simulation scenarios are shown in Fig. 12d and Tab. 1, compared against TLS-measured snow height averaged difference, Northern Transect Magnaprobe snow height averaged difference and SMP-derived snow height differences. For the SNOWPACK simulations, all parameters in the setup were kept the same as in ALPINE3D *R* and C, the only difference is that there is no snow transport available like in the 3D drift simulations.

The TLS-based difference on 4 Feb for the model domain only gives $+0.007$ m, while the Northern transect on 6 Feb gives $+0.042$ m. However, note that when considering a larger area, the TLS increase is approximately $+0.014$ m. If we only choose the section of the transect that is covered by the domain (Fig. 2b), the transect-based increase is $+0.031$ m. Hence, the modeled averaged A3D snow height difference by the end of the simulation period lays between the lowest and highest average values of measurements available. The intermediate transect-based measurement on 30 Jan shows an increase of $+0.012$ m (short section: $+0.009$ m).

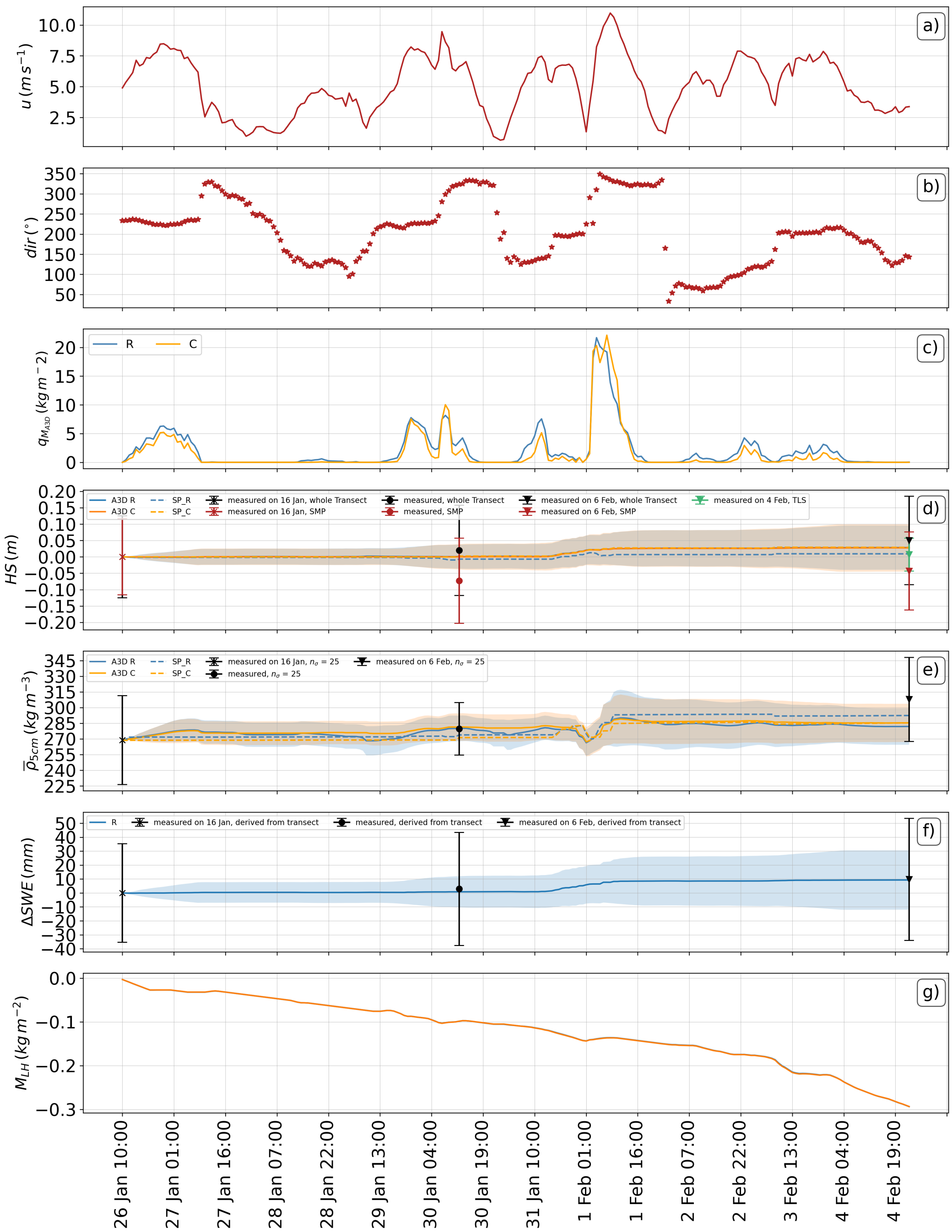

Figure 12. Time series (1h avg) of a) horizontally averaged wind speed (2 m), b) horizontally averaged wind direction (2 m), c) average of absolute deposited and eroded saltation mass per grid cell, d) spatially averaged modeled snow depth and its standard deviation, e) spatially averaged $\overline{\rho}_{5cm}$ modeled snow density, f) cumulative precipitation sum retrieved from KAZR and spatially averaged cumulative $\Delta\, SWE$, g) cumulative sublimated or deposited ice mass (negative = vapor deposition).

One should consider the following measurement uncertainties in this regard: First, note that the low TLS difference is in part due to erosion of snow drifts along the first-year ridge (in the lower left, Fig. 10). However, the transect does not include this ridge, so it misses this erosion. Additionally, it might be possible that the characteristic fluting and scalloping erosional patterns of sastrugi (Filhol & Sturm, 2015) and the steep snow topography of drifts around ridges (e.g., Fig. 11) cause the Magnaprobe measurements to be biased high due to the 25 cm diameter Magnaprobe basket getting propped up on a local high point. In other words, each Magnaprobe observation measures approximately the maximum snow thickness within the basket footprint. However, there are currently no concrete evaluations of this in the literature. Detailed methodological comparison of transect and TLS measurements is beyond the scope of this manuscript and will be investigated in future work.

The standard deviation with time serves as an approximate indicator of snow redistribution over time, making the four drifting snow events clearly visible. However, there is no clear difference between R and C. Based on other simulation results, we can say that if there is a more significant difference in the factors α for τ^*_{th} used, a significant difference is also visible in the standard deviation: with a higher standard deviation for lower τ^*_{th} values. Fig. 2e shows the same as in Fig. 12d but for the average surface density of the first 5 cm of the snowpack ($\overline{\rho}_{5cm}$). A consequence of the decreased snow transport in the C scenario is, that the averaged density is increased over the R scenario. Possible reasons for this are disussed in detail in the next section. Fig. 2f shows the modeled averaged snow-water equivalent (SWE) difference over time, compared with northern transect-derived SWE as reported by Wagner et al. (2022). The mean increase in SWE in the model here is equivalent to the precipitation sum for the same period, which was used as the model input. This is the retrieval based on the Ka-band cloud radar as used in Wagner et al. (2022). It is noteworthy, that although the model shows a slight difference relative to the intermediate measurement, it fits exactly the estimated SWE increase of 9 mm (based on the whole transect). Fig. 12h shows the modeled surface sublimation with time. Negative values corresponds with vapor deposition. Based on this time series, we can rule out the possibility that 1) sublimation occurred at all and 2) that water vapor deposition occurred in relevant amounts that significantly affected the surface mass balance in a positive way.

3.3 Surface snow density

In the following, we compare the modelled snow densities - with a focus on the surface density - with measurements. We compare the surface density rather than the density of the total snowpack because, first, it is relevant to the timing, location and magnitude of the mass of erosion as a function of wind speed and fluid threshold, as described in Section 2.4.5 and Section 2.4.6. Second, the upper centimeters of the snowpack on sea ice often consist of wind slab (Sturm et al., 2002; Merkouriadi et al., 2017), which reduces the horizontal variability of density when averaging vertically. Since we only have 20 individual measurements available with the SMP per measurement day (5 per pit location), we therefore have better comparability with the model using this approach.

3.3.1 Measured snow density

Fig. 13 shows the horizontally averaged snow densities for the snowpack's top 5 cm ($\overline{\rho}_{5cm}$) based on Pit 1 – Pit 4 measured with the SMP (locations shown in Fig. 2), for 16 Jan, 30 Jan and 6 Feb. $\overline{\rho}_{5cm}$ increases from 16 to 30 Jan and then further until 6 Feb. For each day, seen from the surface, a rapid increase in density is observed as the snow depth decreases downwards, followed by a slow decrease. This is probably due to wind slab, a compaction of near-surface snow due to high wind speeds. The minimum is a little bit under $260\,\mathrm{kg\,m^{-3}}$ on 16 Jan while the maximum is $320\,\mathrm{kg\,m^{-3}}$ on 6 Feb. Below the wind slab we find more snow that has undergone temperature gradient metamorphism and thus has a lower density. Similar observations of surface compaction during the MOSAiC expedition were described by Nandan et al. (2022), with even stronger expressions

Parameter	Observation			Model (avg $\pm$ σ)			
	Device / Location	Date	OBS (avg $\pm$ σ)	A3D R	A3D C	SP R	SP C
Δ HS (m)	MP Transect	16 Jan	0	-		(-0.004)	(-0.004)
	SMP	16 Jan					
	TLS	25 Jan	-	0			
	MP Transect	30 Jan	0.02 $\pm$ 0.138	0.001 $\pm$ 0.037	0.0 $\pm$ 0.039	-0.01	0.003
	SMP	30 Jan	-0.07 $\pm$ 0.13				
	TLS	4 Feb	0.007 $\pm$ 0.05	0.028 $\pm$ 0.067	0.028 $\pm$ 0.072	0.006	0.03
	MP Transect	6 Feb	0.05 $\pm$ 0.135	-		0.009	0.033
	SMP	6 Feb	-0.04 $\pm$ 0.119				
$\overline{\rho}_{5cm}$ ($\mathrm{kg\,m^{-3}}$)	SMP	16 Jan	268.9 $\pm$ 42.5	-	-	270.2	270.2
		26 Jan	-	268.6	268.6	268.6	268.6
		30 Jan	279.7 $\pm$ 25.2	280.1 $\pm$ 12.3	281.4 $\pm$ 13.1	272.2	267.0
		4 Feb	-	281.9 $\pm$ 17.5	285.4 $\pm$ 18.3	292.6	272.4
		6 Feb	307.8 $\pm$ 40.3	-	-	293.1	280.3

Table 1. Observed average snow height differences $\Delta\,HS$ derived from the Magnaprobe (MP) measurements along the transect and by TLS differences with time as well as its respective standard deviations σ; observed averaged density of the uppermost 5 cm of the snow cover ($\overline{\rho}_{5cm}$) and its respective standard deviation over time, derived from the SMP along the transect, and the corresponding values from the modeled ALPINE3D (A3D) R and C scenarios and modeled SNOWPACK (SP) R and C scenarios. The bracketed negative values of the SP scenarios on Jan 16 represent the difference in the Jan 26 value minus the Jan 16 value for illustrative purposes, although the values themselves cannot be used for comparisons with the A3D model.

measured at a different location - a few hundred meters away a few weeks earlier, in November as well as early December.

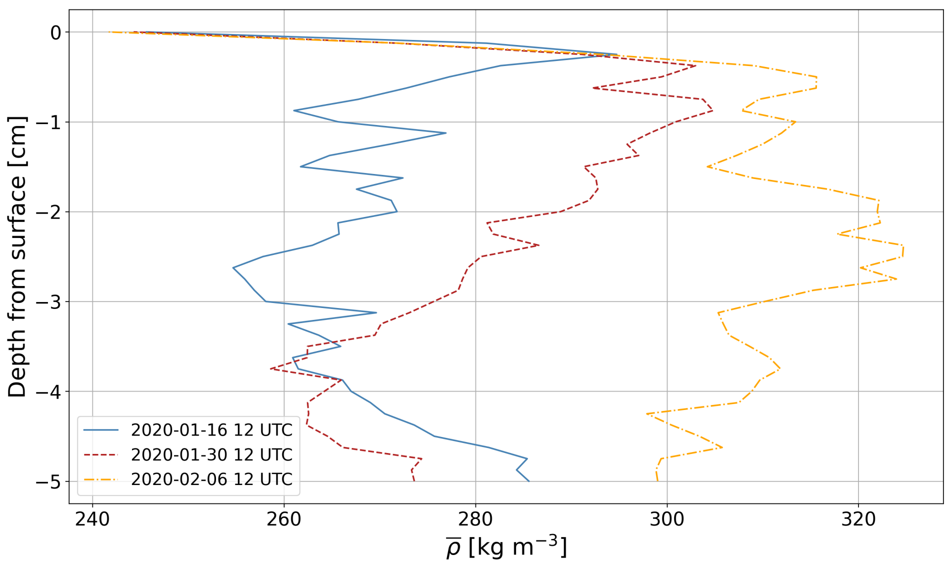

Figure 13. Horizontally averaged snow surface density profiles (5 cm depth) from snow pit 1-4 over time. Zero denotes the snow surface.

Fig. 14a confirms that for most of the pits, $\overline{\rho}_{5cm}$ increases with time, and increases for all pits averaged from around 270 kg m^{-3} on 30 Jan to 308 kg m^{-3} on 6 Feb. In contrast to the surface density, however, the total density (Fig. 14b) shows a somewhat different picture: While for $\overline{\rho}_{5cm}$, the average density increases from 16 Jan to 30 Jan from 270 kg m^{-3} by 10 kg m^{-3} to around 280 kg m^{-3} (Tab. 1), the average density for the whole profile decreases first slightly below 280 kg m^{-3} and then increases to little over 290 kg m^{-3}. Most interestingly, for the whole profile, the spread is strongly reduced on 30 Jan, compared to the spread before (16 Jan) and after (6 Feb). This is likely due to the fact that net erosion has occurred from the respective areas of the 4 snow pits: Mean snow depths derived from SMP measurements have decreased at each individual pit between 16 and 30 Feb, namely -0.85 cm at Pit 1, -17.2 cm at Pit 2, -9.6 cm at Pit 3, and -2.0 cm at Pit 4. This results in an average decrease of 7.4 cm. When we look at our initial snow profile on 16 Jan (Fig. 4) and the snow densities of the upper 5 cm (Fig. 14), it becomes clear that the decrease in density is probably attributed, at least partially, to erosion of the upper layers. However, it is also likely that snowfall at low wind speeds contributed to a reduction in density, as well, which occurred between 29 and 30 Jan (Fig. 12g). In contrast to 30 Jan, the mean density of the entire profile increased between 16 Jan and 6 Feb. At the same time, the mean height has decreased, but only by 4.3 cm on average. This corresponds to an increase of 3 cm compared to 30 Jan.

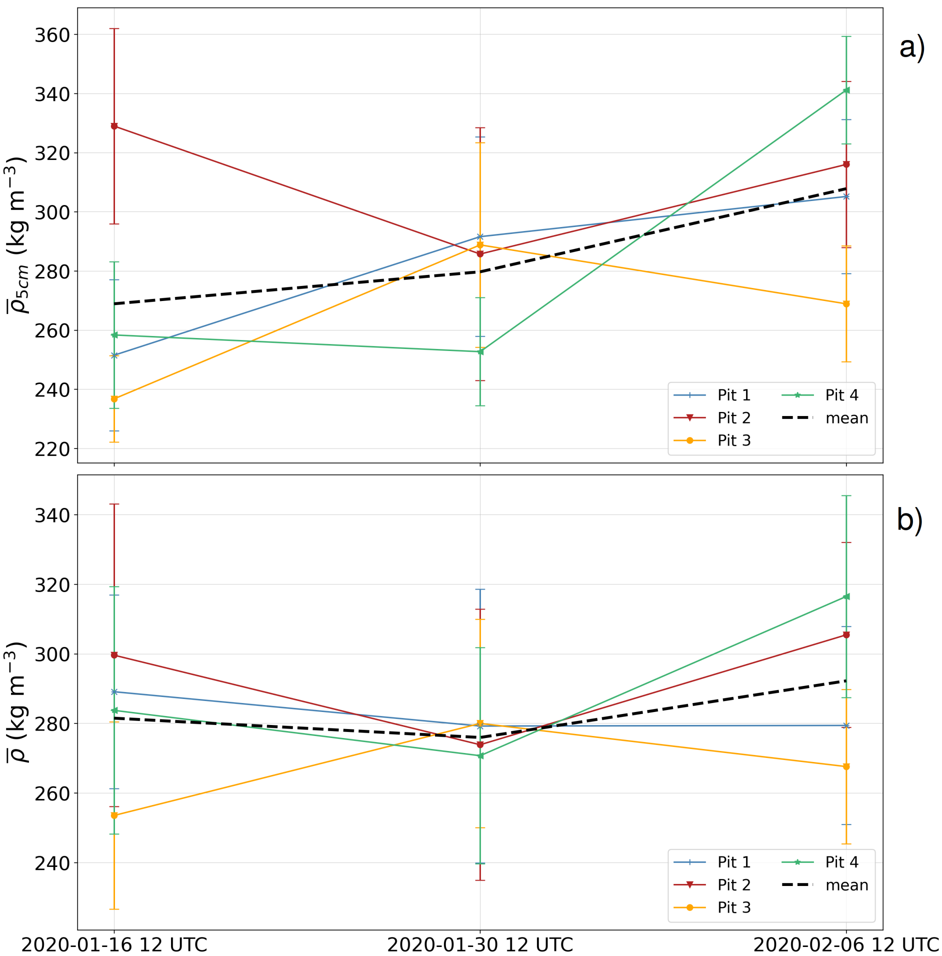

Figure 14. a) Averaged snow surface densities (upper 5 cm) for snow pits 1–4. The black dashed line notes the total average over time. Error bars show the corresponding upper and lower limit for the standard deviation at each pit location at each time. b) same as in a) but averaged for the whole vertical profile.

3.3.2 Modeled snow density

We now analyse if the model is able to reproduce the $\overline{\rho}_{5cm}$ increase with time found in the manual snow pits. Spatially modeled snow density fields for the top 5 cm of the snowpack, $\overline{\rho}_{5cm}$, for R and C simulations, respectively, are shown in Fig.10c and Fig.10d. Spatial differences of the density between R and C are visible. For the C scenario, the density is higher on average, and the surface appears smoother, while for the R scenario, the spatial variation appears larger with lower maximum densities.

As discussed in the previous section, the smaller fluid threshold in scenario R increases snow transport and consequently increases the spatial snow distribution. There is also a significant increase in $\overline{\rho}_{5cm}$ with time (Fig. 12e, Tab. 1). SMP-based horizontally averaged $\overline{\rho}_{5cm}$ and their respective standard deviations are shown for 16 Jan, 30 Jan and 6 Feb in the same figure. Most of the time, in the C scenario, the surface density is slightly higher. While during the first event the densities increase to approximately the same value of slightly over 280 kg m^{-3}. Subsequently, the R scenario density drops to lower values. At a later time, during the snowfall event, the densities are almost equal again, and this behaviour continues. At the beginning of the simulation period, the density is about the same as the measurements on 16 Jan (269 kg m^{-3}). The reason for this is that the 1-D SNOWPACK model was initiated with the density measurements on 16 Jan, and during the spin-up period of 10 days until 26 Jan (Fig. 4). Accordingly, the surface density remained about the same between 16 Jan and 26 Jan (which also justifies a comparison of the measurements from 16 Jan with the model on 26 Jan, also regarding snow depth and SWE). On 30 Jan, the measured average is 280 kg m^{-3}, which is well captured by the R scenario, where the C scenario models slightly too high values. By the end of the simulation, neither simulation correctly reproduces the averaged measured density (308 kg m^{-3}); however, both models are within the lower standard deviation of the measurement. The R scenario generally shows a stronger variability of the density with time, in particular it shows stronger decreases in the intermediate time. Here, we note that the modeled average surface density may decrease significantly with time due to 3 reasons:

1. Due to snowfall during low wind speeds, which produces low density layers on top.
2. When at certain locations in the domain the wind speed is sufficient to generate snow transport, i.e. when the threshold friction velocity $u*_{th}$ is exceed, while at the same time, the deposited snow density function (Equation 1) computes relatively low densities for the re-deposition of the snow that has been eroded from high-density surfaces. This might lead to a decrease, on average.
3. When erosion may expose lighter layers lower down in the snow cover.

The difference between the R and C simulations is attributed to point 2, as the snowfall rate and wind speed are identical for both scenarios. An increased $u*_{th}$ leads to less re-distribution and hence less fluctuation in the density. However, the significant drop of $\overline{\rho}_{5cm}$ for both scenarios - R and C - is attributed to snowfall (explained under point 1 above), as snowfall occurred before the wind started on 1 Feb. Interestingly, $\overline{\rho}_{5cm}$ of the R and C scenario converge during the subsequent event with the highest measured wind speed on 1 Feb, which occurred under significant snowfall conditions.

3.3.3 Comparison with 1-D SNOWPACK simulations

To evaluate whether a time- and computationally intensive calculation with ALPINE3D gives an advantage in terms of averaged properties over very short time and low computationally intensive 1-dimensional simulations, we compared two SNOWPACK simulations, R_SP and C_SP with ALPINE3D *R* and *C*. The $\overline{\rho}_{5cm}$ time series shown in Fig. 12e), reveal that neither of the two SNOWPACK setups is able to simulate the $\overline{\rho}_{5cm}$ increase on 30 Jan 1200 UTC. For the measurement at this time, the density is underestimated for SP_R by 8 kg m^{-3} and for SP_C by 13 kg m^{-3}. In contrast to that, the R and C scenarios of ALPINE3D show an excellent agreement for $\overline{\rho}_{5cm}$ with the measurements at this time. However, by the end of the simulation period neither one of the A3D simulations nor one of the SNOWPACK simulations captures the average measured density accurately. However, SP_R is closest to the measured $\overline{\rho}_{5cm}$, while SP_C is similar to C. This is somewhat surprising, as intuitively, we would have expected that a decreased fluid threshold would lead to more erosion, and consequently a decreased $\overline{\rho}_{5cm}$.

Unlike the A3D setups, neither of the SNOWPACK simulations shows lots of variability with time. All of the modeled densities lay within the lower standard deviation of the measured density. While the differences in results between SP_R and SP_C are quite high at the end of the simulation time, they are smaller for the same change in the α parameter. Based on these findings, one could perhaps argue that using ALPINE3D with the snowdrift module reduces the probability of being way off in the results. The temporal fluctuation of $\overline{\rho}_{5cm}$ in the ALPINE3D setups may not seem realistic, but it is at least as questionable how likely it is that - as simulated by SNOWPACK - there is almost no fluctuation except for very punctual events.

3.4 Cross sections

In a final step, we evaluate the model in terms of snow deposition in detailed cross sections. Cross sections in typical wind-erosion/deposition areas allow for a detailed investigation, for instance in terms of snow height, grain ratios, snow age, density or thermal conductivity. This is particularly interesting when considering that the model in its current state does not form dunes on level areas. In addition, considering that ridges are main accumulation zones, the cross sections might show a potential to investigate thermodynamic ice growth in these areas in future work. The located cross sections are shown in Fig. 11 as sections 1–3 (S1–S3)

3.4.1 S1

S1 is the cross section where the model reproduced erosion and deposition in best agreement with TLS measurements (Fig. 15a). It is noteworthy that this section is characterized first and foremost by the fact that it is aligned approximately 90° to a distinct pressure ridge of about 1 m height. The model reproduces here the snow depth difference very well, and the most pronounced difference is that it computes a sharp accumulation peak on top of the ridge that is not seen in the measurements (Fig. 15a). On the other hand, the model also reproduces the depth decrease at approximately 10 m distance.

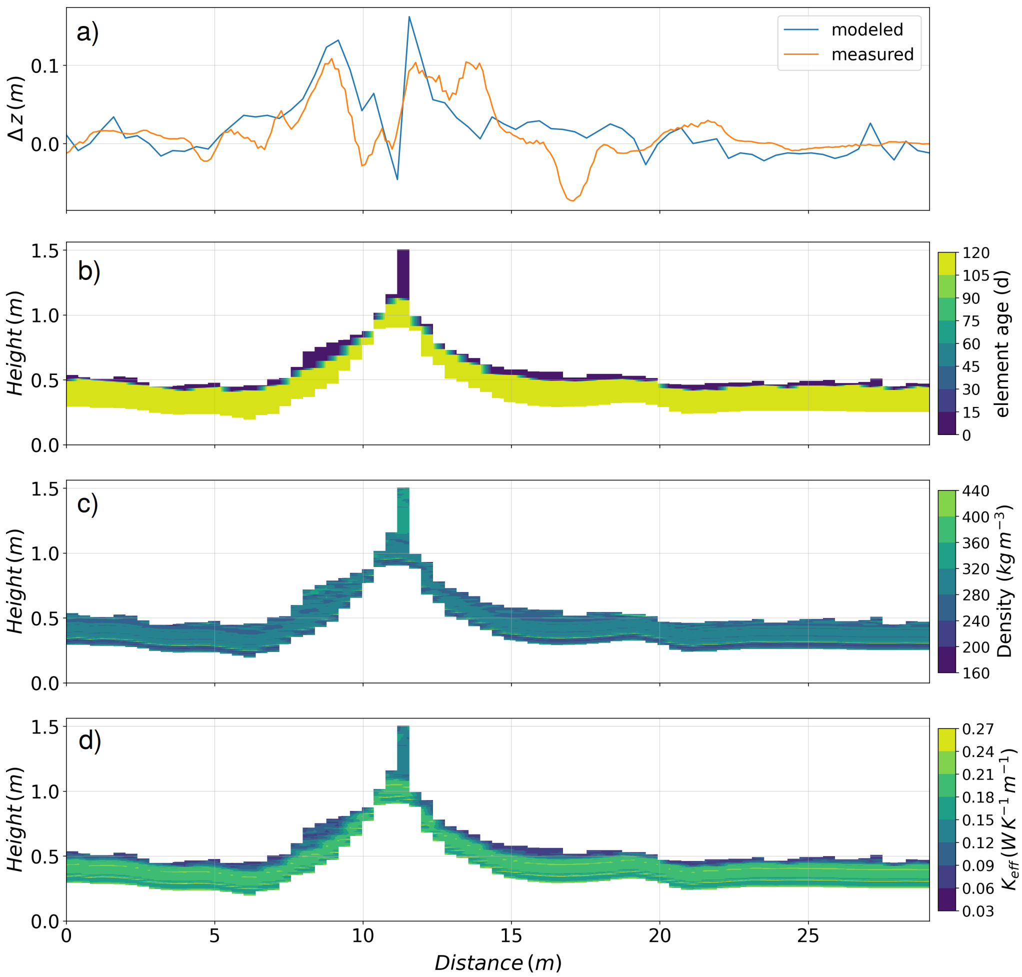

Figure 15. Cross section plots related to cross section 1 (S1) of the reference simulation (R), as shown in Fig. 11, of a) snow depth difference (4 Feb – 25 Jan) of the model output and TLS, b) snow age, c) snow density and d) thermal conductivity of snow.

Fig. 15d shows that most of the snow has been accumulated in approximately the last three days in the model run, which corresponds to the time period 1 – 4 Feb. For the same period, the highest densities of deposited snow are computed (Fig. 15c).

Detailed computed thermal conductivities (Fig. 15d) show the potential of the model. The modeled values of the deposited snow on top are probably too low here, as Macfarlane et al. (2023) found an time-and spatial average K_{eff} of 0.25 ± 0.05 W K^{-1} m^{-1} for MOSAiC. Reasons for the low modeled K_{eff} are not known at this time, and need to be researched further. Macfarlane et al. (2023) also state that the thermal conductivity of snow around ridges does not significantly differ from snow on level areas, however, they found that the thermal resistance instead was about 3 times higher on ridges areas and they conclude that therefore ridges should be separately considered for modeling. This finding and the ability of our model to represent the thermal properties of snow in spatial detail reinforces our approach.

The detailed cross section 2 is shown in Fig. 16. While on the ridged area right to the highest point of the ridge at approximately 18 cm distance, the model accumulates too much snow, the snow height is accurately modeled left of the ridge peak (Fig. 16a).

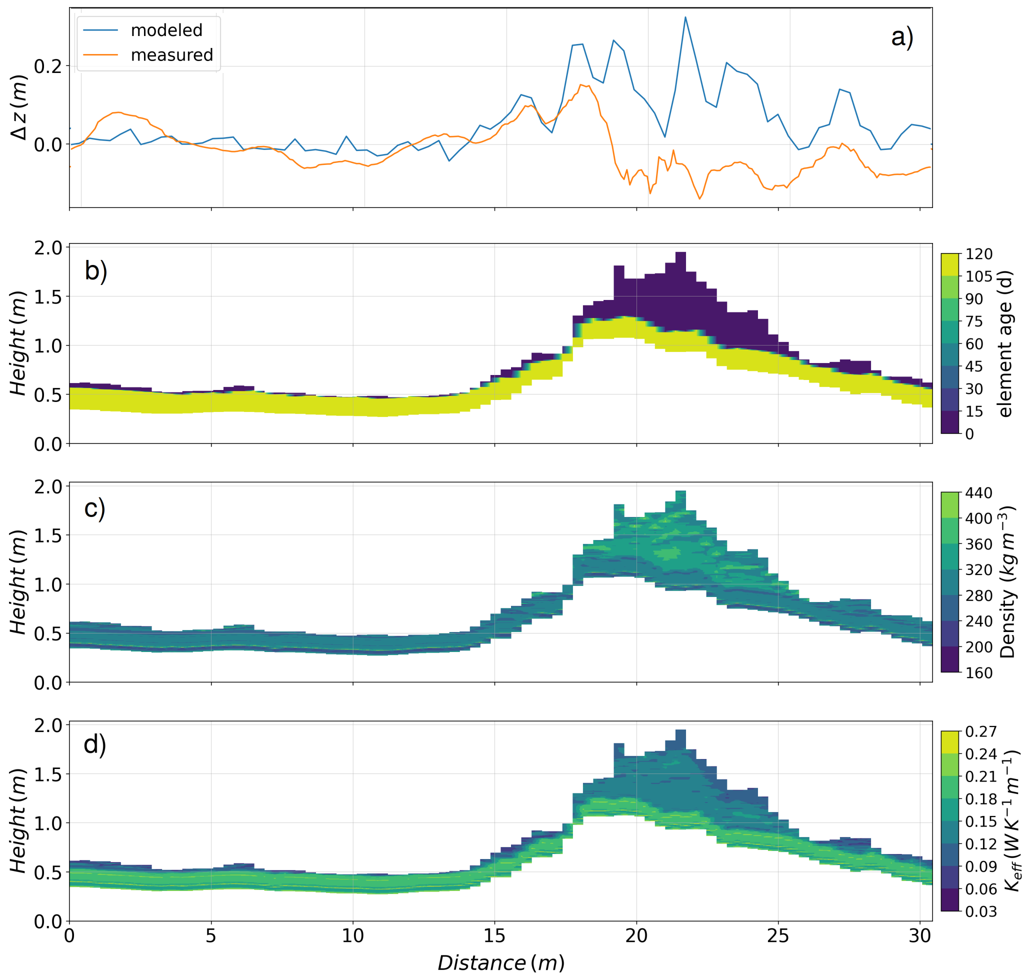

Figure 16. As in Fig. 15, but for cross section S2 as shown in Fig. 11.

The colours in the snow age (Fig. 16a) indicate, that most of the deposition occurred during one event. In the large accumulation between around 17 and 20 m distance, a strong spatial variability in density is observed (Fig. 16c), clearly showing the increased density of the freshly deposited snow. K_{eff} (Fig. 16d) again shows quite low values which need to be investigated. The large snow accumulation highlights why the thermal resistance can be large around ridges (Macfarlane et al., 2023).

In cross section 3, we wanted to investigate the highly variable accumulation in form of waves that was observed (Fig. 11b,d). The spatial variablity of the measurement is seen in Fig. 17a. The model does not model these highly accurately, however, it appears like there is a correlation, and that mainly the phase is shifted, especially for the first 10 m. Generally, the model reproduces here the differences well. Fig. 17b reveals that the snow accumulation occurred much more homogeneously compared to cross section 1 and 2. This shows that a flat surface tends to lead to more homogeneous accumulation, contrary to ridged areas.

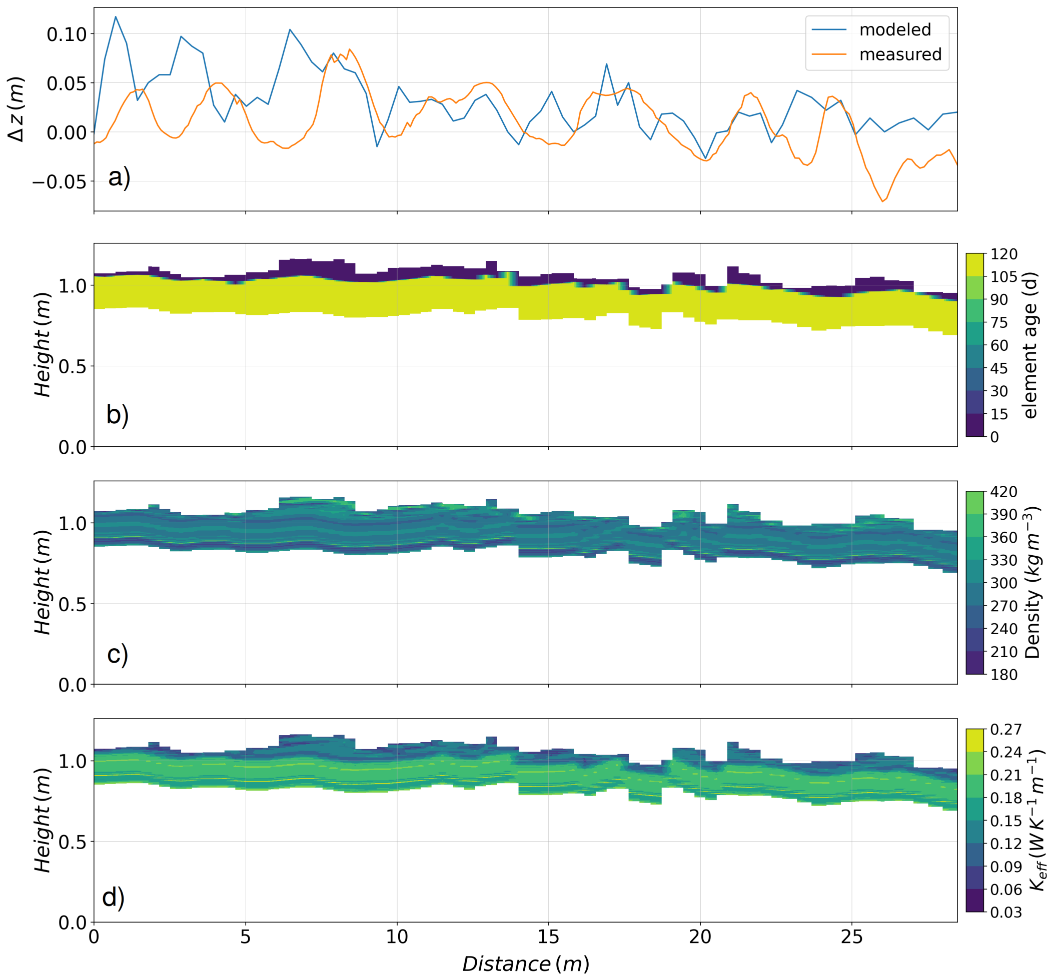

Figure 17. As in Fig. 15, but for cross section S3 as shown in Fig. 11.

The density (Fig. 17c) and thermal conductivity (Fig. 17d) reveal not many large conspicuities compared to cross section 1 and cross section 2.

4 Conclusions and Outlook

We applied the 3D-snow cover-atmosphere model ALPINE3D with the drifting snow module to Arctic sea ice for the first time, for an area of 100 x 100 m. The fitted model simulated a 10-day simulation period in which the model would be fed by measurement data collected during the winter of the Multidisciplinary drifting Observatory for the Study of Arctic Climate expedition (MOSAiC). A digital elevation model (DEM) was used as the underlying topography, based on terrestrial laser scans (TLS) conducted during the expedition. As wind field input, we used RANS steady state wind fields computed with OpenFOAM based on in-situ measurements of wind speed and direction, collected on a meterological tower. Other measurement data from and around the tower used to drive the model were air temperature, relative humidity and incoming longwave radiation. Snow depth and detailed snow density measurements were used to initialise and evaluate the model. For comparison of the modelled mass fluxes, horizontal mass fluxes derived from a Snow Particle Counter (SPC) measurement at the meteorological tower were used. After calibration, we conducted a a sensitivity study, with respect to an increased fluid threshold. In addition, we made comparisons with 1-D SNOWPACK simulations. A detailed study of spatio-temporal snow-redistribution and surface snow densification has been conducted. Finally, detailed snow profiles along three selected cross sections in the domain were investigated.

The model shows a very good timing for snow transport compared to measurements and estimates relative mass fluxes well with high correlation of $r = 0.92$. The histograms of the snow depth differences do not deviate largely from the measurements, but when using an increased fluid threshold, the compression of the distribution gets significantly decreased - which is due to a reduced wind-induced transport of snow. When looking at the spatial correlation in the form of a semi-variogram, it is noticeable that generally the modeled semi-variance is significantly higher than the measured - however, the range of 6 m is about the same for both the model and the measurements. Interestingly, Liston et al. (2018) also found a range of 6 m (for measurements of absolute height), and Sturm et al. (2002) found values at least close to 6 m. The initially strongly increasing semi-variance in the model in the lower range is probably due to the missing generation of dunes, which can be clearly seen in the measurements. Using time series of statistical snow distribution, we were able to visualize the wind-induced redistribution of snow. These show that significantly less snow redistribution occurs when the fluid threshold is increased. While in the reference simulation redistribution occurs almost continuously, in the comparison scenario redistribution can essentially be reduced to the four events that stand out clearly from the measurements. The qualitative comparisons between model and measurements show that dunes are hardly formed in the model, which is probably due to a missing dynamic mesh in the model, as the near-surface wind field does not adapt to the freshly deposited snow from the previous period. However, there are some areas where the model reproduces the accumulation excellently, and even if on a very small scale matches do not necessarily prevail, the model calculates large amounts of snow - as in the measurements - in the ridged areas. Erosion occurs in the model, but is generally underestimated compared to the measurements.

The time course of the spatially averaged surface density of the upper 5 cm shows that wind slab formed, with a value of 269 kg m−3 on 16 Jan, 280 kg m−3 on 30 Jan, and 307.8 kg m−3 on 6 Feb, becoming increasingly stronger. The averaged density over the entire profile, unlike the surface density, shows a decrease at 30 Jan, while it increases again at 6 Feb. The reason is probably that as erosion increased, the density fraction of layers below, consisting mostly of depth hoar or faceted grains, increased relatively within the mean. The averaged surface density in the model is excellently reproduced at 30 Jan, but at 6 Feb it is underestimated by 26 kg in the reference and by 22 kg in the comparison, although both modeled means are still within the standard deviation of the measurements. SNOWPACK, on the other hand, models a too low density at 30 Jan (referne underestimated by 15 kg; comparison underestimated by 13 kg), while it is closer to the measurements, at least with α of 3.0 at 6 Feb (reference underestimated by 8 kg; comparison underestimated by 28 kg). The temporal variation of the density is significantly higher for ALPINE3D than for SNOWPACK, which is especially the case for the reference. The strong decreases in densities at times are rather unrealistic and due to the fact that in the current settings the model erodes too easily at low fluid threshold, and then calculates too low densities with the given density parameterization for just deposited snow, which corresponds to a decrease in density on average. Overall, the differences between the two ALPINE3D setups are smaller than between the two SNOWPACK setups, leading us to conclude that using an ALPINE3D drifting snow setup reduces the likelihood of being wrong with an adjusted fluid threshold.

The cross sections reveal details of deposition and erosion, both in terms of height differences between model and simulation, as well as spatially high-resolution parameters, such as age of the deposited snow, density, or thermal conductivity. For the selected cross sections 1-3, the model simulates the snow depth differences extremely well for the most part, especially for cross section 1. However, the visible correlations in cross sections 2 and 3, as well as the accurately calculated snow depth difference left of the ridge cross section 2 are also remarkable. The observed waves in cross section 3 are not clearly reproduced, but it is apparently phase-shifted at a similar wave-length. The snow age in the cross sections allows to investigate when the snow has settled. The density in the cross sections reveal stronger spatial variations for the snow that has accumulated over time. The plots of the effective thermal conductivity show - even if the conductivity of the freshly deposited snow appearss too high (under the assumption of drifting snow) - how the effects of the snow cover on sea ice growth in ridged areas could be investigated.

Our adjusted ALPINE3D setup using the snowdrift routine with RANS wind fields and a high resolution sea ice topography, allows for detailed investigation of the Arctic snow cover. For the first time, snow redistribution on sea ice is modelled in dependence of temporally varying detailed snow properties. This approach could be particularly relevant for modeling during highly variable weather, e.g., storms or warm air intrusions (Liston et al., 2007), because it then causes the microstructure of the snow surface to change significantly with time due to sintering. An Arctic undergoing major climatic changes with increasing temperatures increases this demand. We see several applications as well as further developments in the future. A combination of our setup with the sea ice variant of ALPINE3D (Wever et al., 2020, 2021) could allow a detailed study of the spatial variability of the thermodynamically driven growth and melt of sea ice. By studying our cross sections, we have already shown an approach to conduct this, e.g., it would be possible to study the effect of the effective thermal conductivity of snow on the ice growth on and around pressure ridges. Furthermore, we believe that a dynamic mesh would again greatly improve the model, allowing for dune formation. In combination with the general approach to study sea ice mass balances, this would be of great relevance e.g. for the formation of melt ponds (Petrich et al., 2012; Lecomte et al., 2015). However, dunes could also be generated, for example, within a sub-model using a cellular automaton (Sharma et al., 2019).

5 Open Research

A3D and SNOWPACK Setup data (include OpenFOAM generated wind fields) are available at https://doi.org/10.5281/zenodo.7723224 (Wagner & Lehning, 2023). TLS point clouds can be obtained from https://arcticdata.io/data/10.18739/A26688K9D/ (Clemens-Sewall et al., 2023). The flux tower wind measurements can be downloaded from

ftp://ftp2.psl.noaa.gov/Projects/MOSAiC/tower/3_level_archive/level3.4/ (Cox et al., 2023). KAZR data can be obtained from the ARM data center: https://doi.org/10.5439/1498936 (Lindenmaier et al., 2020). All SMP profiles are available on https://doi.org/10.1594/PANGAEA.935554 (Macfarlane et al., 2021). Transect Magnaprobe snow depths can be downloaded from https://doi.org/10.1594/PANGAEA.937781 (Itkin et al., 2021). SWE derived from Transect and SMP can be downloaded under https://doi.pangaea.de/10.1594/PANGAEA.927460 (Wagner et al., 2021). Preliminary SPC data can be obtained from https://doi.org/10.5281/zenodo.7715728 (Wagner & Frey, 2023). Source code for the adjusted ALPINE3D model can be obtained from https://gitlabext.wsl.ch/snow-models/alpine3d.git under the "alpine3d_mosaic" branch. Source code for the adjusted SNOWPACK model can be obtained from https://gitlabext.wsl.ch/snow-models/snowpack.git under the "snowpack_mosaic" branch. The source code for OpenFOAM® v2106 can be downloaded from https://develop.openfoam.com/Development/openfoam.git.

Acknowledgments

David N. Wagner and Michael Lehning were supported by the Swiss National Science Foundation (grant no. SNSF-200020_179130). Martin Schneebeli, Amy R. Macfarlane and David N. Wagner were supported by the Swiss Polar Institute (grant no. DIRCR-2018-003). Martin Schneebeli and Amy R. Macfarlane were supported by the European Union's Horizon 2020 research and innovation program projects ARICE (grant no. 730965) for berth fees associated with the participation of the DEARice project and the WSL

Institute for Snow and Avalanche Research SLF (grant no. WSL_201812N1678). David Clemens-Sewall was supported by NSF OPP-1724540. Matthew D. Shupe was supported by the DOE Atmospheric System Research Program (grant nos. DE-SC0019251 and DE-SC0021341). Data used in this paper were produced as part of the international Multidisciplinary drifting Observatory for the Study of the Arctic Climate (MOSAiC) with the tag MOSAIC20192020 and the project ID: AWI_PS122_00. Met tower data were supported by the National Science Foundation (grant no. OPP-1724551) and by NOAA's Physical Sciences Laboratory (PSL) and Global Ocean Monitoring and Observing Program (GOMO). KAZR reflectivities for precipitation retrieval were obtained from the Atmospheric Radiation Measurement (ARM) user facility, a U.S. Department of Energy (DOE) Office of Science user facility managed by the Biological and Environmental Research Program. The authors thank all MOSAiC participants for contributing to the paper in one way or another: the MOSAiC logistics team, the ship's personnel, all the different team members (ICE, ATMOS, BGC, ECO, OCEAN), the ARM crew, the project coordination and the MOSAiC project board. We also refer to the extended acknowledgement for MOSAiC (Nixdorf et al., 2021). We thank Daniel Kükenbrink for the helpful information on proper point cloud processing with open source software.

References

Bagnold, R. A. (1941). *The physics of blown sand and desert dunes / by r.a. bagnold* [Book]. William Morrow New York.

Bartelt, P., & Lehning, M. (2002). A physical SNOWPACK model for the Swiss avalanche warning Part I: numerical model. *Cold Regions Science and Technology*, *35*(3), 123–145. doi: 10.1016/s0165-232x(02)00074-5

Blackford, J. R. (2007, oct). Sintering and microstructure of ice: a review. *Journal of Physics D: Applied Physics*, *40*(21), R355–R385. Retrieved from `https://doi.org/10.1088%2F0022-3727%2F40%2F21%2Fr02` doi: 10.1088/0022-3727/40/21/r02

Clemens-Sewall, D., Polashenski, C., Raphael, I., Perovich, D., Fons, S., Itkin, P., ... Svavarsdottir, S. (2023). *High-resolution repeat topography of drifting ice floes in the arctic ocean from terrestrial laser scanning collected on the multidisciplinary drifting observatory for the study of arctic climate expedition.* [Data set]. (Arctic Data Center.) doi: 10.18739/A26688K9D

Clifton, A., Rüedi, J.-D., & Lehning, M. (2006). Snow saltation threshold measurements in a drifting-snow wind tunnel. *Journal of Glaciology*, *52*(179), 585–596. doi: 10.3189/172756506781828430

CloudCompare. (2023). *Cloudcompare source code.* Retrieved from `https://github.com/CloudCompare/CloudCompare`

Colbeck, S. (1998). Sintering in a dry snow cover. *Journal of Applied Physics*, *84*(8), 4585-4589. Retrieved from `https://doi.org/10.1063/1.368684` doi: 10.1063/1.368684

Colbeck, S., of Engineers, U. S. A. C., Research, C. R., & (U.S.), E. L. (1997). *A review of sintering in seasonal snow.* U.S. Army Cold Regions Research and Engineering Laboratory. Retrieved from `https://books.google.ch/books?id=D\_CHKAAACAAJ`

Conrad, O., Bechtel, B., Bock, M., Dietrich, H., Fischer, E., Gerlitz, L., ... Böhner, J. (2015). System for automated geoscientific analyses (saga) v. 2.1.4. *Geoscientific Model Development*, *8*(7), 1991–2007. Retrieved from `https://gmd.copernicus.org/articles/8/1991/2015/` doi: 10.5194/gmd-8-1991-2015

Cox, C., Gallagher, M., Shupe, M., Persson, O., Solomon, A., Fairall, C., ... Uttal, T. (2023). *Continuous observations of the surface energy budget and meteorology over the arctic sea ice during mosaic.* (Multidisciplinary Drifting Observatory for the Study of Arctic Climate (MOSAiC), central Arctic, October 2019 -

September 2020. Scientific Data. Submitted.) doi: 10.18739/A2PV6B83F

Déry, S. J., & Tremblay, L.-B. (2004). Modeling the effects of wind redistribution on the snow mass budget of polar sea ice. *Journal of Physical Oceanography*, *34*(1), 258-271. Retrieved from https://doi.org/10.1175/1520-0485(2004)034<0258:MTEOWR>2.0.CO;2 doi: 10.1175/1520-0485(2004)034⟨0258:MTEOWR⟩2.0.CO;2

Doorschot, J. J. J., & Lehning, M. (2002). Equilibrium saltation: Mass fluxes, aerodynamic entrainment, and dependence on grain properties. *Boundary-Layer Meteorology*, *104*(1), 111–130. doi: 10.1023/a:1015516420286

Doorschot, J. J. J., Lehning, M., & Vrouwe, A. (2004, Dec 01). Field measurements of snow-drift threshold and mass fluxes, and related model simulations. *Boundary-Layer Meteorology*, *113*(3), 347–368. Retrieved from https://doi.org/10.1007/s10546-004-8659-z doi: 10.1007/s10546-004-8659-z

Fierz, C., Armstrong, R., Durand, Y., Etchevers, P., Greene, E., Mcclung, D., ... Sokratov, S. (2008, 09). The 2008 international classification of seasonal snow on the ground. In (p. 579–580).

Filhol, S., & Sturm, M. (2015). Snow bedforms: A review, new data, and a formation model. *Journal of Geophysical Research: Earth Surface*, *120*(9), 1645-1669. Retrieved from https://agupubs.onlinelibrary.wiley.com/doi/abs/10.1002/2015JF003529 doi: https://doi.org/10.1002/2015JF003529

Gerber, F., Lehning, M., Hoch, S. W., & Mott, R. (2017). A close-ridge small-scale atmospheric flow field and its influence on snow accumulation. *Journal of Geophysical Research: Atmospheres*, *122*(15), 7737-7754. Retrieved from https://agupubs.onlinelibrary.wiley.com/doi/abs/10.1002/2016JD026258 doi: https://doi.org/10.1002/2016JD026258

Groot Zwaaftink, C. D., Cagnati, A., Crepaz, A., Fierz, C., Macelloni, G., Valt, M., & Lehning, M. (2013, 02). Event-driven deposition of snow on the antarctic plateau: Analyzing field measurements with snowpack. *The Cryosphere, Volume 7, Issue 1, 2013, pp.333-347*, *7*, 333-347. doi: 10.5194/tc-7-333-2013

Groot Zwaaftink, C. D., Diebold, M., Horender, S., Overney, J., Lieberherr, G., Parlange, M. B., & Lehning, M. (2014, Oct 01). Modelling small-scale drifting snow with a lagrangian stochastic model based on large-eddy simulations. *Boundary-Layer Meteorology*, *153*(1), 117–139. Retrieved from https://doi.org/10.1007/s10546-014-9934-2 doi: 10.1007/s10546-014-9934-2

Hames, O., Jafari, M., Wagner, D. N., Raphael, I., Clemens-Sewall, D., Polashenski, C., ... Lehning, M. (2022). Modeling the small-scale deposition of snow onto structured arctic sea ice during a mosaic storm using snowbedfoam 1.0. *Geoscientific Model Development*, *15*(16), 6429–6449. Retrieved from https://gmd.copernicus.org/articles/15/6429/2022/ doi: 10.5194/gmd-15-6429-2022

Itkin, P., Webster, M., Hendricks, S., Oggier, M., Jaggi, M., Ricker, R., ... Liston, G. E. (2021). *Magnaprobe snow and melt pond depth measurements from the 2019-2020 mosaic expedition.* (PANGAEA) doi: 10.1594/PANGAEA.937781

Juretic, F., Philippose, R., & Clifford, I. (2021). *cfmesh source code.* Retrieved from https://sourceforge.net/p/cfmesh/code/ci/development/tree/

Keenan, E., Wever, N., Dattler, M., Lenaerts, J. T. M., Medley, B., Kuipers Munneke, P., & Reijmer, C. (2021). Physics-based snowpack model improves representation of near-surface antarctic snow and firn density. *The Cryosphere*, *15*(2), 1065–1085. Retrieved from https://tc.copernicus.org/articles/15/1065/2021/ doi: 10.5194/tc-15-1065-2021

King, J., Howell, S., Brady, M., Toose, P., Derksen, C., Haas, C., & Beckers, J. (2020). Local-scale variability of snow density on Arctic sea ice. *The Cryosphere*, *14*(12), 4323–4339. doi: 10.5194/tc-14-4323-2020

Lecomte, O., Fichefet, T., Flocco, D., Schroeder, D., & Vancoppenolle, M. (2015). Interactions between wind-blown snow redistribution and melt ponds in a coupled ocean–sea ice model. *Ocean Modelling*, *87*, 67-80. Retrieved from https://www.sciencedirect.com/science/article/pii/S1463500314001784 doi: https://doi.org/10.1016/j.ocemod.2014.12.003

Lee, S., Wolberg, G., & Shin, S. (1997). Scattered data interpolation with multilevel b-splines. *IEEE Transactions on Visualization and Computer Graphics*, *3*(3), 228-244. doi: 10.1109/2945.620490

Lehning, M., Bartelt, P., Brown, B., Fierz, C., & Satyawali, P. (2002). A physical snowpack model for the swiss avalanche warning: Part ii. snow microstructure. *Cold Regions Science and Technology*, *35*(3), 147 - 167. Retrieved from http://www.sciencedirect.com/science/article/pii/S0165232X02000733 doi: https://doi.org/10.1016/S0165-232X(02)00073-3

Lehning, M., Bartelt, P., Brown, B., Russi, T., Stöckli, U., & Zimmerli, M. (1999). snowpack model calculations for avalanche warning based upon a new network of weather and snow stations. *Cold Regions Science and Technology*, *30*(1), 145 - 157. Retrieved from http://www.sciencedirect.com/science/article/pii/S0165232X99000221 doi: https://doi.org/10.1016/S0165-232X(99)00022-1

Lehning, M., Löwe, H., Ryser, M., & Raderschall, N. (2008). Inhomogeneous precipitation distribution and snow transport in steep terrain. *Water Resources Research*, *44*(7). Retrieved from https://agupubs.onlinelibrary.wiley.com/doi/abs/10.1029/2007WR006545 doi: 10.1029/2007WR006545

Lehning, M., Völksch, I., Gustafsson, D., Nguyen, T. A., Stähli, M., & Zappa, M. (2006). Alpine3d: a detailed model of mountain surface processes and its application to snow hydrology. *Hydrological Processes*, *20*(10), 2111-2128. Retrieved from https://onlinelibrary.wiley.com/doi/abs/10.1002/hyp.6204 doi: 10.1002/hyp.6204

Leonard, K. C., & Maksym, T. (2011). The importance of wind-blown snow redistribution to snow accumulation on bellingshausen sea ice. *Annals of Glaciology*, *52*(57), 271–278. doi: 10.3189/172756411795931651

Li, L., & Pomeroy, J. W. (1997). Estimates of Threshold Wind Speeds for Snow Transport Using Meteorological Data. *Journal of Applied Meteorology*, *36*(3), 205–213. doi: 10.1175/1520-0450(1997)036⟨0205:eotwsf⟩2.0.co;2

Lindenmaier, I., Nelson, D., Isom, B., Hardin, J., Matthews, A., Wendler, T., & Castro, V. (2020). *Ka arm zenith radar (kazrcfrge).* (Atmospheric Radiation Measurement (ARM) user facility.) doi: 10.5439/1498936

Liston, G. E., & Elder, K. (2006a). A distributed snow-evolution modeling system (snowmodel). *Journal of Hydrometeorology*, *7*(6), 1259-1276. Retrieved from https://doi.org/10.1175/JHM548.1 doi: 10.1175/JHM548.1

Liston, G. E., & Elder, K. (2006b). A Meteorological Distribution System for High-Resolution Terrestrial Modeling (MicroMet). *Journal of Hydrometeorology*, *7*(2), 217–234. doi: 10.1175/jhm486.1

Liston, G. E., Haehnel, R. B., Sturm, M., Hiemstra, C. A., Berezovskaya, S., & Tabler, R. D. (2007). Simulating complex snow distributions in windy environments using snowtran-3d. *Journal of Glaciology*, *53*(181), 241–256. doi: 10.3189/172756507782202865

Liston, G. E., Itkin, P., Stroeve, J., Tschudi, M., Stewart, J. S., Pedersen, S. H., … Elder, K. (2020). A lagrangian snow-evolution system for sea-ice applications (snowmodel-lg): Part i—model description. *Journal of Geophysical Research: Oceans*, *125*(10), e2019JC015913. Retrieved from https://agupubs.onlinelibrary.wiley.com/doi/abs/10.1029/2019JC015913 (e2019JC015913 2019JC015913) doi: https://doi.org/10.1029/2019JC015913

Liston, G. E., Polashenski, C., Rösel, A., Itkin, P., King, J., Merkouriadi, I., & Haapala, J. (2018). A distributed snow-evolution model for sea-ice applications (snowmodel). *Journal of Geophysical Research: Oceans*, *123*(5), 3786-3810. Retrieved from https://agupubs.onlinelibrary.wiley.com/doi/abs/

10.1002/2017JC013706 doi: 10.1002/2017JC013706

Liston, G. E., & Sturm, M. (1998). A snow-transport model for complex terrain. *Journal of Glaciology*, *44*(148), 498–516. doi: 10.3189/S0022143000002021

Macfarlane, A. R., Löwe, H., Gimenes, L., Wagner, D. N., Dadic, R., Ottersberg, R., ... Schneebeli, M. (2023). Thermal conductivity of snow on arctic sea ice. *EGUsphere*, *2023*, 1–22. Retrieved from https://egusphere.copernicus.org/preprints/egusphere-2023-83/ doi: 10.5194/egusphere-2023-83

Macfarlane, A. R., Schneebeli, M., Dadic, R., Wagner, D. N., Arndt, S., Clemens-Sewall, D., ... Tavri, A. (2021). Snowpit SnowMicroPen (SMP) force profiles collected during the MOSAiC expedition [data set]. PANGAEA. Retrieved from https://doi.org/10.1594/PANGAEA.935554 (In: Macfarlane, AR et al. (2021): Snowpit raw data collected during the MOSAiC expedition. PANGAEA, https://doi.org/10.1594/PANGAEA.935934) doi: 10.1594/PANGAEA.935554

Mälicke, M. (2022). Scikit-gstat 1.0: a scipy-flavored geostatistical variogram estimation toolbox written in python. *Geoscientific Model Development*, *15*(6), 2505–2532. Retrieved from https://gmd.copernicus.org/articles/15/2505/2022/ doi: 10.5194/gmd-15-2505-2022

Matheron, G. (1963, 12). Principles of geostatistics. *Economic Geology*, *58*(8), 1246-1266. Retrieved from https://doi.org/10.2113/gsecongeo.58.8.1246 doi: 10.2113/gsecongeo.58.8.1246

Matrosov, S. Y. (2007). Modeling Backscatter Properties of Snowfall at Millimeter Wavelengths. *Journal of the Atmospheric Sciences*, *64*(5), 1727–1736. doi: 10.1175/jas3904.1

Matrosov, S. Y., Shupe, M. D., & Djalalova, I. V. (2008). Snowfall Retrievals Using Millimeter-Wavelength Cloud Radars. *Journal of Applied Meteorology and Climatology*, *47*(3), 769–777. doi: 10.1175/2007jamc1768.1

Matrosov, S. Y., Shupe, M. D., & Uttal, T. (2022, 04). High temporal resolution estimates of Arctic snowfall rates emphasizing gauge and radar-based retrievals from the MOSAiC expedition. *Elementa: Science of the Anthropocene*, *10*(1). Retrieved from https://doi.org/10.1525/elementa.2021.00101 (00101) doi: 10.1525/elementa.2021.00101

Melo, D. B., Sharma, V., Comola, F., Sigmund, A., & Lehning, M. (2021). Modeling snow saltation: the effect of grain size and interparticle cohesion. *Earth and Space Science Open Archive*, 29. Retrieved from https://doi.org/10.1002/essoar.10507087.1 doi: 10.1002/essoar.10507087.1

Merkouriadi, I., Gallet, J.-C., Graham, R. M., Liston, G. E., Polashenski, C., Rösel, A., & Gerland, S. (2017). Winter snow conditions on arctic sea ice north of svalbard during the norwegian young sea ice (n-ice2015) expedition. *Journal of Geophysical Research: Atmospheres*, *122*(20), 10,837-10,854. Retrieved from https://agupubs.onlinelibrary.wiley.com/doi/abs/10.1002/2017JD026753 doi: 10.1002/2017JD026753

Mott, R., Schirmer, M., Bavay, M., Grünewald, T., & Lehning, M. (2010). Understanding snow-transport processes shaping the mountain snow-cover. *The Cryosphere*, *4*(4), 545–559. Retrieved from https://www.the-cryosphere.net/4/545/2010/ doi: 10.5194/tc-4-545-2010

Nandan, V., Willatt, R., Mallett, R., Stroeve, J., Geldsetzer, T., Scharien, R., ... Hoppman, M. (2022). Wind transport of snow impacts ka- and ku-band radar signatures on arctic sea ice. *The Cryosphere Discussions*, *2022*, 1–38. Retrieved from https://tc.copernicus.org/preprints/tc-2022-116/ doi: 10.5194/tc-2022-116

Nicolaus, M., Haas, C., Bareiss, J., & Willmes, S. (2006). A model study of differences of snow thinning on arctic and antarctic first-year sea ice during spring and summer. *Annals of Glaciology*, *44*, 147–153. doi: 10.3189/172756406781811312

Nicolaus, M., Perovich, D., Spreen, G., Granskog, M., Albedyll, L., Angelopoulos, M., ... Wendisch, M. (2021). Overview of the mosaic expedition - snow and sea ice. *Elementa: Science of the Anthropocene*, *9*. Retrieved from `https://doi.org/10.1525/elementa.2021.000046` doi: 10.1525/elementa.2021.000046

Nixdorf, U., Dethloff, K., Rex, M., Shupe, M., Sommerfeld, A., Perovich, D. K., ... Boetius, A. (2021, September). *Mosaic extended acknowledgement.* Zenodo. Retrieved from `https://doi.org/10.5281/zenodo.5541624` doi: 10.5281/zenodo.5541624

Persson, P. O. G. (2012). Onset and end of the summer melt season over sea ice: thermal structure and surface energy perspective from SHEBA. *Climate Dynamics*, *39*(6), 1349–1371. doi: 10.1007/s00382-011-1196-9

Persson, P. O. G., Shupe, M. D., Perovich, D., & Solomon, A. (2017). Linking atmospheric synoptic transport, cloud phase, surface energy fluxes, and sea-ice growth: observations of midwinter SHEBA conditions. *Climate Dynamics*, *49*(4), 1341–1364. doi: 10.1007/s00382-016-3383-1

Petrich, C., Eicken, H., Polashenski, C. M., Sturm, M., Harbeck, J. P., Perovich, D. K., & Finnegan, D. C. (2012). Snow dunes: A controlling factor of melt pond distribution on arctic sea ice. *Journal of Geophysical Research: Oceans*, *117*(C9). Retrieved from `https://agupubs.onlinelibrary.wiley.com/doi/abs/10.1029/2012JC008192` doi: https://doi.org/10.1029/2012JC008192

Pomeroy, J. W., & Gray, D. M. (1990). Saltation of snow. *Water Resources Research*, *26*(7), 1583-1594. Retrieved from `https://agupubs.onlinelibrary.wiley.com/doi/abs/10.1029/WR026i007p01583` doi: https://doi.org/10.1029/WR026i007p01583

Schlögl, S., Marty, C., Bavay, M., & Lehning, M. (2016). Sensitivity of alpine3d modeled snow cover to modifications in dem resolution, station coverage and meteorological input quantities. *Environmental Modelling Software*, *83*, 387-396. Retrieved from `https://www.sciencedirect.com/science/article/pii/S1364815216300378` doi: https://doi.org/10.1016/j.envsoft.2016.02.017

Schmidt, J. (2014). *terrainblockmesher.* GitHub. Retrieved from `https://github.com/jonasIWES/terrainBlockMesher` (IWESOL - IWES Open Library, Fraunhofer IWES, Oldenburg, Germany)

Schmidt, R. A. (1980). Threshold wind-speeds and elastic impact in snow transport. *Journal of Glaciology*, *26*(94), 453–467. doi: 10.3189/S0022143000010972

Schneebeli, M., & Johnson, J. B. (1998). A constant-speed penetrometer for high-resolution snow stratigraphy. *Annals of Glaciology*, *26*, 107–111. doi: 10.3189/1998AoG26-1-107-111

Selige, T., Böhner, J., & Ringeler, A. (2006, 01). Processing of srtm x-sar data to correct interferometric elevation models for land surface applications. *Göttinger Geographische Abhandlungen*, *115*.

Sharma, V., Braud, L., & Lehning, M. (2019). Understanding snow bedform formation by adding sintering to a cellular automata model. *The Cryosphere*, *13*(12), 3239–3260. Retrieved from `https://www.the-cryosphere.net/13/3239/2019/` doi: 10.5194/tc-13-3239-2019

Shupe, M., Chu, D., Costa, D., Cox, C., Creamean, J., de Boer, G., ... Wagner, D. (2021, 6). Multidisciplinary drifting observatory for the study of arctic climate (mosaic) (field campaign report). Retrieved from `https://www.osti.gov/biblio/1787856` doi: 10.2172/1787856

Shupe, M., Rex, M., Blomquist, B., Persson, P., Schmale, J., Uttal, T., ... Yue, F. (2022). Overview of the mosaic expedition—atmosphere. *Elementa: Science of the Anthropocene*, *10*(1). doi: 10.1525/elementa.2021.00060

Steger, C. R., Reijmer, C. H., van den Broeke, M. R., Wever, N., Forster, R. R., Koenig, L. S., ... Noël, B. P. Y. (2017). Firn meltwater retention on the greenland ice sheet: A model comparison. *Frontiers in Earth Science*, *5*,

3. Retrieved from https://www.frontiersin.org/article/10.3389/feart.2017.00003 doi: 10.3389/feart.2017.00003

Sturm, M., & Holmgren, J. (2018). An Automatic Snow Depth Probe for Field Validation Campaigns. *Water Resources Research*, *54*(11), 9695–9701. doi: 10.1029/2018wr023559

Sturm, M., Holmgren, J., & Perovich, D. K. (2002). Winter snow cover on the sea ice of the arctic ocean at the surface heat budget of the arctic ocean (sheba): Temporal evolution and spatial variability. *Journal of Geophysical Research: Oceans*, *107*(C10), SHE 23-1-SHE 23-17. Retrieved from https://agupubs.onlinelibrary.wiley.com/doi/abs/10.1029/2000JC000400 doi: 10.1029/2000JC000400

Sturm, M., & Massom, R. A. (2016). Snow in the sea ice system: friend or foe? In *Sea ice* (p. 65-109). John Wiley and Sons, Ltd. Retrieved from https://onlinelibrary.wiley.com/doi/abs/10.1002/9781118778371.ch3 doi: 10.1002/9781118778371.ch3

Sullivan, C. B., & Kaszynski, A. (2019, May). PyVista: 3D plotting and mesh analysis through a streamlined interface for the Visualization Toolkit (VTK). *Journal of Open Source Software*, *4*(37), 1450. Retrieved from https://doi.org/10.21105/joss.01450 doi: 10.21105/joss.01450

Vosselman, G. (2000, 01). Slope based filtering of laser altimetry data. *IAPRS*, *XXXIII*.

Wagner, D. N., & Frey, M. M. (2023, March). *Preliminary data of drifting snow mass flux from the lower SPC at MOSAiC (2020-01-26 to 2020-02-04) for the submitted paper "Towards a fully physical representation of snow on Arctic sea ice using a 3D snow-atmosphere model"* [dataset]. Zenodo. Retrieved from https://doi.org/10.5281/zenodo.7715728 doi: 10.5281/zenodo.7715728

Wagner, D. N., Jaggi, M., Macfarlane, A. R., Arndt, S., Krampe, D., Regnery, J., … Schneebeli, M. (2021). *Snow water equivalent retrievals from snowmicropen data from mosaic leg 1 - leg 3.* (PANGAEA) doi: 10.1594/PANGAEA.927460

Wagner, D. N., & Lehning, M. (2023, March). *Preliminary DOI/Repository of ALPINE3D and SNOWPACK data of the submitted paper "Towards a fully physical representation of snow on Arctic sea ice using a 3D snow-atmosphere model"* [dataset]. Zenodo. Retrieved from https://doi.org/10.5281/zenodo.7723224 doi: 10.5281/zenodo.7723224

Wagner, D. N., Shupe, M. D., Cox, C., Persson, O. G., Uttal, T., Frey, M. M., … Lehning, M. (2022). Snowfall and snow accumulation during the mosaic winter and spring seasons. *The Cryosphere*, *16*(6), 2373–2402. Retrieved from https://tc.copernicus.org/articles/16/2373/2022/ doi: 10.5194/tc-16-2373-2022

Webster, M. A., Rigor, I. G., Nghiem, S. V., Kurtz, N. T., Farrell, S. L., Perovich, D. K., & Sturm, M. (2014). Interdecadal changes in snow depth on arctic sea ice. *Journal of Geophysical Research: Oceans*, *119*(8), 5395-5406. Retrieved from https://agupubs.onlinelibrary.wiley.com/doi/abs/10.1002/2014JC009985 doi: https://doi.org/10.1002/2014JC009985

Weiss, A. I., King, J., Lachlan-Cope, T., & Ladkin, R. (2011). On the effective aerodynamic and scalar roughness length of weddell sea ice. *Journal of Geophysical Research: Atmospheres*, *116*(D19). Retrieved from https://agupubs.onlinelibrary.wiley.com/doi/abs/10.1029/2011JD015949 doi: 10.1029/2011JD015949

Weller, H. G., Tabor, G., Jasak, H., & Fureby, C. (1998). A tensorial approach to computational continuum mechanics using object-oriented techniques. *Computers in Physics*, *12*(6), 620. doi: 10.1063/1.168744

Wever, N., Leonard, K., Maksym, T., White, S., Proksch, M., & Lenaerts, J. T. M. (2021). Spatially distributed simulations of the effect of snow on mass balance and flooding of antarctic sea ice. *Journal of Glaciology*, *67*(266), 1055–1073.

doi: 10.1017/jog.2021.54
Wever, N., Rossmann, L., Maaß, N., Leonard, K. C., Kaleschke, L., Nicolaus, M., & Lehning, M. (2020). Version 1 of a sea ice module for the physics-based, detailed, multi-layer snowpack model. *Geoscientific Model Development*, *13*(1), 99–119. Retrieved from https://www.geosci-model-dev.net/13/99/2020/ doi: 10.5194/gmd-13-99-2020
Widener, K., Bharadwaj, N., & Johnson, K. (2012). *Ka-Band ARM Zenith Radar (KAZR) Handbook.* (Tech. Rep.). (ARM user facility. DOE/SC-ARM/TR-106.)
Zhang, W., Qi, J., Wan, P., Wang, H., Xie, D., Wang, X., & Yan, G. (2016). An easy-to-use airborne lidar data filtering method based on cloth simulation. *Remote Sensing*, *8*(6). Retrieved from https://www.mdpi.com/2072-4292/8/6/501 doi: 10.3390/rs8060501